University of Waterloo

Faculty of Engineering

Nanotechnology Engineering

NE 408: Nanosystems Design Project

Identifier: NE_2018_06

Title: Wireless Power Transfer for Implantable Medical Devices

Final Report

March 23, 2018

This report is submitted as the final report requirement of the NE 409 course. It has been written solely by us and has not been submitted for academic credit before (other than appendices A-G) at this or any other academic institution.

Team members

Adam Weinstein (awweinst@edu.uwaterloo.ca) 20512898

Dhilan Bekah (d2bekah@edu.uwaterloo.ca) 20512356

Graham Joe (g2joe@edu.uwaterloo.ca) 20524639

Kai Slaughter (kvslaugh@edu.uwaterloo.ca) 20509911

Nayera El-Sawah (nelsawah@edu.uwaterloo.ca) 20508049

Design Project Consultant

Dr. Omar Ramahi, Professor
Electrical and Computer Engineering

Executive Summary

Medical treatment tailored to individual characteristics, or personalized medicine, has undergone a recent paradigm shift due to advances in the fields of nanomaterials, medical imaging, and biotechnology [1]. Coupled with increases in computational power and the advent of mobile and wireless technologies, sensors have become central to personalized medicine. Implantable biosensors have revolutionized medical treatment and monitoring systems due to their ability to detect events occurring in the body in real-time [2], allowing for more timely treatment and appropriate remedies, potentially leading to improved quality of life and life expectancy [2]. The size of products requiring power has primarily been limited by battery power density [3]. Significant investments have been made in order to develop smaller and lighter batteries, and consequently medical devices [3]. An alternative method of powering implantable devices involves the use of wireless power transfer (WPT) technology. Near-field inductive coupling technology currently dominates biomedical applications of WPT due to its high power transfer efficiency, but is limited to short distance transmission and requires relatively large coils [4]. These limitations lead to more invasive powering of implantable biosensors and larger device sizes.

The proposed Fourth Year Design Project (FYDP) applies far-field radio-frequency (RF) WPT technology for implantable biosensors. In this project, a rectifying antenna and diode system, referred to as a 'rectenna', is proposed as a power delivery system [5]. While this system includes both a transmitting and a receiving unit, the focus of this design is on the receiving unit. This WPT system bypasses the need for a battery, shrinking device size significantly and reducing the need for invasive surgeries.

The powering system is designed for eventual incorporation into existing implantable biomedical devices and would be sold to manufacturers of these devices. Additional target customers for the envisioned product are individuals who require an implantable biomedical device, as well as medical professionals who may recommend the device to patients. Key requirements include intrinsic device safety, compliance with appropriate regulations, ease of integration into patient life (comfort), minimal medical intervention, durability, and low cost.

To meet these requirements, functional specifications are formulated with regards to comfort, safety, robustness, and cost. Comfort can be achieved by ensuring that the device is small and can operate unobtrusively. A planar antenna can be fabricated directly onto unused device surfaces, effectively eliminating the space allocated for a battery. In accordance with regulatory guidelines for maximum power density of radiation in the frequency range of the device, the maximum power output from the transmitting unit will be limited to 0.8 W [6]. In combination with the transmission behaviour of microwave radiation in the frequency range of interest, the minimum power efficiency of the rectenna that is required for successful device operation through biological tissue was found to be 10%. Biocompatible encasing will ultimately be used to ensure high corrosion resistance of greater than 98% when compared to surgical stainless steel. Finally, while the cost of the rectenna powering unit should generally not exceed the cost of current battery technology, there may be a startup cost associated with technology development; this can be justified by performance improvements.

Design specifications were formulated considering the aforementioned functional specifications. An operating frequency of 12 GHz was chosen, as it was demonstrated to sufficiently penetrate biological tissue [7] and results in an acceptably small device size. A design for 5.8 GHz operation was selected from literature as a design prototype for its high efficiency and reduced size [8]. A verification of the system's characteristics and performance was conducted by simulation and then by experiment before modifying the design to suit the purposes of the targeted application. This design employs a stepped impedance

dipole antenna for absorption of microwaves, and an interdigital capacitor, diode and chip capacitor for signal rectification from alternating current (AC) to direct current (DC). Electromagnetic wave antenna simulations were performed using COMSOL and demonstrated peak absorption near the frequency interest. Impedance characteristics of the antenna were determined and imported into Advanced Design System (ADS) for rectifying circuit simulations. Through this analysis, the optimal frequency was confirmed to be 5.8 GHz and the rectification efficiency was determined to be about 32%.

Microfabrication techniques were implemented to fabricate devices on a glass wafer, and involved aluminum deposition, photolithography, and aluminum etching. Discrete circuit components were attached to the device using silver epoxy. In order to characterize fabricated devices, testing plans were developed and attempted. The testing setup consisted of a signal generator connected to a horn antenna, which transmitted microwave radiation to the rectenna device. A voltmeter was connected across the transmission lines of the device to measure the DC voltage to determine the received and rectified signal. This testing plan included characterizing an isolated antenna for impedance characteristics and resonant frequency and a series of optimization steps for power, frequency and load resistance. Upon implementing the testing plan, there was no measurable voltage across the device.

The report outlines several future steps that could be taken to successfully implement a device meeting the desired functional requirements. This includes using a power amplifier to determine if higher power levels are required for the device, choosing a diode with a lower turn-on voltage to enable lower power operation, and further optimizing rectification circuitry for increased impedance matching. Additionally, alternative designs could be considered to achieve higher efficiency at low power, including an array design. Overall, this report demonstrates the potential of this rectenna device for powering biomedical implants through simulations and outlines the steps necessary for further validation and optimization.

Acknowledgements

We would like to thank Ahmed Ashoor and Ahmed Abdel Aziz, graduate students whose guidance was instrumental in the progress of the project in terms of antenna, simulation, and microfabrication knowledge. We would also like to thank Luis Gutierrez and Professor Raafat Mansour, Manager and Director, respectively of the Centre for Integrated RF Engineering (CIRFE) for granting us access to the CIRFE cleanroom to perform parts of the device fabrication. The group would also like to thank Rossi Ivanova and Czang-Ho Lee of the Nanotechnology Undergraduate Cleanroom for granting cleanroom access, substrates, and guidance on microfabrication processes. We extend our thanks to Dr. Bill Jolley, Lab Director, Research and Special Projects, for aiding in the connection of discrete components to the devices. Characterization equipment was kindly provided by Professor Safieddin Safavi-Naeini and Dr. Gholamreza Rafi, Director and Assistant Director, respectively of the Centre for Intelligent Antenna Radio Systems. We would also like to thank Neutronics Solutions for providing free samples of MA4E1317 diodes that were used in the final prototype.

Glossary of Terms and Acronyms

AC: Alternating current

ADS: Advanced Design System; used for RF and circuit simulations

CCRPB: Consumer and Clinical Radiation Protection Bureau

COMSOL: Computer Solutions, commercial multiphysics simulation software build on the finite element method (FEM)

Coplanar stripline (CPS): Planar transmission lines consisting of two metallic strips separated by a gap on a substrate, where one of the strips acts as the electric ground instead of a ground plane

DC: Direct current

DMM: Digital multimeter, and instrument used to measure DC voltages

HFSS: High Frequency Structure Simulator

ISM band: The industrial, scientific, and medical radio band; refers to parts of the RF and microwave spectrum reserved for industrial, scientific, and medical applications rather than for communications

Lumped Port: Type of boundary condition in COMSOL Electromagnetic Waves module. Serves as a lumped model of circuit components, from which wave excitation can occur.

MA4E1316: Model name of a Schottky barrier diode

Perfect Electric Conductor (PEC): Type of boundary condition in electromagnetic simulations; models a material with no resistance, hence closely approximating metallic materials

Perfectly Matched Layer (PML): Artificial absorbing layer for wave equations used to truncate computational regions to simulate problems with open boundaries. Designed so that waves incident upon PML from a non-PML medium do not reflect at the interface.

Rectenna: A rectifying antenna system. Consists of an antenna to transduce microwaves into AC electrical current and a rectifying circuit to convert AC power into DC power

RF: Radio frequency, sometimes loosely used to also encompass the microwave frequency regime (20 kHz - 300 GHz)

RSA: real-time spectrum analyzer

S-parameters: Scattering parameters; quantify how energy propagates through a multi-port network. For example, S_{ij} is the ratio of the amplitude of the signal output from port j to the amplitude to the signal incident on port i. S_{ii} represents a reflection coefficient, and S_{ij} where i and j are not equal represent transmission coefficients.

S_{11}: A measure of signal reflectance; typically used to assess antenna and circuit efficiency

S_{21}: A measure of signal transmittance

WPT: Wireless power transfer

Via: Conductive metal filling that connects circuit elements on different planes of a multi-planar device

VNA: vector network analyzer

Table of Contents

Team members 2
Design Project Consultant 2
Executive Summary 3
Acknowledgements 5
Glossary of Terms and Acronyms 6
List of Figures 10
List of Tables 12
1 Introduction 13
2 Societal & Environmental Impact 13
3 Project Milestones 14
4 Customer Requirements 14
5 Functional Specifications 15
6 Design Specifications 16
7 Verification Plan 17
8 Testing Plan 17
9 Verification Data 18
    Simulation Setup 18
    Simulation Results 19
10 Prototype Construction 24
    Step 1: Mask Design 24
    Step 2: Cleanroom Fabrication 25
    Step 3: Discrete Component Soldering 26
11 Testing Results 28
12 Future Steps 29
Appendix A: Customer Requirements 31
    Safety 31
    Regulatory Compliance 31
    Undetectable to Patient 31
    Easy Implantation with Minimal Medical Intervention 31
    Long Lifetime and Robustness 32
    Low Cost 32
Appendix B: Project Plan and Milestones 33
    Design and Simulations 33

Material Acquisition 33
Fabrication 33
Characterization 34
Data Analysis 34
Reports 34
Symposium 35
Human Resources 35
Timeline 36
Appendix C: Functional Specifications 37
Safety 37
Comfort 37
Robustness 38
Cost 38
Summary 38
Appendix D: Verification Plan for the Paper Design 39
Appendix E: Test Plan for the Constructed Prototype 40
Appendix F: Design Specifications 41
Background 41
Antenna Array Project Design 43
Fabrication 45
Background 45
Design for Photolithographic Fabrication 46
Fabrication Protocol 47
Safety 48
Cost 48
Appendix G: Verification Data 49
Reproduction of previous work 49
Scaled-down design – COMSOL 53
Appendix H: Prototype Test Data 57
References 58

List of Figures

Figure 6-1: Design schematic from [8] 17

Figure 9-1: Antenna dimensions 18

Figure 9-2: Boundary conditions in the COMSOL antenna simulations 18

Figure 9-3: ADS schematic for the rectification circuit 19

Figure 9-4: COMSOL antenna simulation on Duroid substrate; a) S11 vs Frequency and b) Impedance vs Frequency plots 20

Figure 9-5: a) Resistance vs Frequency and b) Reactance vs Frequency plots presented in [8] for the antenna design 20

Figure 9-6: Rectification efficiency response to incident power sweep 21

Figure 9-7: ADS rectification circuit simulation on Duroid substrate; a) S11 vs Frequency and b) Rectification Efficiency vs Frequency plots 21

Figure 9-8: COMSOL antenna simulation on silica substrate; a) S11 vs Frequency and b) Impedance vs Frequency plots 22

Figure 9-9: ADS rectification circuit simulation on silica substrate; a) S11 vs Frequency and b) Rectification Efficiency vs Frequency plots 22

Figure 9-10: COMSOL scaled-down antenna simulation on silica substrate; a) S11 vs Frequency and b) Impedance vs Frequency plots 23

Figure 9-11: ADS scaled-down rectification circuit simulation on silica substrate; a) S11 vs Frequency and b) Rectification Efficiency vs Frequency plots 23

Figure 10-1: Mask design for fabricated rectenna devices 24

Figure 10-2: Dimensions of the fabricated antenna 25

Figure 10-3: Microfabrication steps 25

Figure 10-4: Component attachment, viewed through a microscope lens; a) diode; b) capacitor 27

Figure E-1: Testing plan 40

Figure F-1: Schematic showing the super cell of metamaterial absorber [23] 41

Figure F-2: Schematic showing the feeding network (right) and the locations of the connecting vias on the metasurface (left) [23] 42

Figure F-3: Electric field magnitude surface plot of the metamaterial super cell for different orthogonal polarizations [23] 42

Figure F-4: Exploded-view of device layers..... 43

Figure F-5:Layers of device fabricated in [23]..... 45

Figure F-6: a) the design of the feeding network (not to scale). b) a single antenna component (measurements in millimeters). c) the entire supercell (measurements in millimeters). d) the feed network to scale. e) the supercell and feed network on the same plane..... 47

Figure G-1: Simulated structure (units of μm). Supercell is shown on top of a layer of dielectric backed by a PEC. On top of the metamaterial is an air box, at the top of which is the source excitation, and a PML air box..... 49

Figure G-2: a) Absorption spectrum from [23]; the plots for both polarizations are very similar, so only one polarization is shown. b) Reproduced absorption spectrum for polarization 1. c) Reproduced absorption spectrum for polarization 2. 50

Figure G-3: a) Efficiency spectrum from [23]; the plots for both polarizations are very similar, so only one polarization is shown. b) Reproduced efficiency spectrum for polarization 1. c) Reproduced efficiency spectrum for polarization 2. 51

Figure G-4: a) Reproduced surface plot of the magnitude of the electric field at the resonant frequency for polarization 1. b) Reproduced surface plot of the magnitude of the electric field at the resonant frequency for polarization 2..... 51

Figure G-5: Schematic of matching network in ADS [23]..... 52

Figure G-6: a) S-parameter vs. frequency plot for each polarization from [23]. b) Reproduced S-parameter vs. frequency plot for each polarization. c) Efficiency vs. frequency plot for each polarization from [23]. d) Reproduced efficiency vs. Frequency plot for each..... 53

Figure G-7: Lumped port impedance sweep for scaled down system..... 54

Figure G-8: a) Polarization 1 absorption spectrum. b) Polarization 2 absorption spectrum..... 54

Figure G-9: a) Polarization 1 efficiency spectrum. b) Polarization 2 efficiency spectrum. 55

Figure G-10: a) Polarization 1 electric field. b) Polarization 2 electric field..... 55

Figure G-11 : a) Polarization 1 VSWR. b) Polarization 2 VSWR 56

Figure H-1: a) Backing for device testing. b) Close-up of device probing for measurement. c) Horn antenna. d) Anechoic chamber setup 57

List of Tables

Table B-1: Human resources 35

Table B-2: Timeline 36

Table C-1: Summary of functional specifications 38

Table G-1: Dimensions for scaled-down design (see Figure F1 for parameter definitions) 54

1 Introduction

Increasingly advanced technology for personalized medicine has introduced demand for safe and reliable methods to power implantable medical devices, including sensors and treatment modalities [9]. Currently, implantable devices are powered by batteries. As trends in medical devices continue towards being more thin and flexible, a reduction in volume has been one of the primary focuses [10]. However, constraints on the achievable energy density of batteries limit the size reduction of implantable devices. There is an inherent tradeoff between device scale-down and power, resulting from difficulties in maintaining a high power density as the size is reduced [10]. Additionally, the limited lifetime of batteries in devices such as pacemakers necessitates their replacement by invasive surgery.

Taking these design challenges into consideration, this project proposes an alternative method for powering such implantable medical devices. It is possible to transfer power through free space, and even through dielectric media such as the human body, by utilizing electromagnetic radiation. Antennas are well known devices for wireless electronic signal communications, they can emit or collection radio and microwave frequency electromagnetic radiation. This process can similarly be used to transfer power. By intelligently designing an antenna system with the addition of a few electrical components, it is possible to convert a signal communication system into an efficient wireless power transfer (WPT) system. As a result, WPT could be used to power implantable medical devices by using a source external to the human body to power at a distance.

2 Societal & Environmental Impact

The proposed project presents several benefits with regards to societal impact, as the design has a direct application to the field of medicine and patient care. The environmental impact of this device should be comparable to current electronic device production standards, with the added benefit of eliminating hazardous waste associated with batteries. The value of this design project lies in the ability to directly power an implantable medical device using far-field transmission technology, bypassing the need for a battery. This project is a proof of principle aiming to demonstrate that sufficient power for such a device can be delivered remotely via harvesting of microwave radiation. This technology has the potential to be applied to miniaturized biosensors as well, which can lead to improved patient care.

3 Project Milestones

Several milestones were outlined for the duration of this project in order to manage and successfully achieve the project goals. These milestones provide a solid infrastructure for the development of the project. Referring to *Appendix B*, the Design and Simulations milestone was at the core of the project, with the aim of achieving a design that was possible to fabricate and that had a theoretical efficiency of greater than or equal to 10%. This was partly achieved, since a device was successfully fabricated based on simulations, and a theoretical rectification efficiency of ~35% was demonstrated. The frequency of operation for the fabricated device, however, was not 12 GHz as originally envisioned, but 5.8 GHz instead, since scale-down was not successfully performed prior to the deadline for fabrication. The necessary materials and components for fabrication of the device were successfully acquired well within the allocated budget. Following this, the device was successfully fabricated using metal sputtering and photolithography as planned, however, copper was replaced with aluminum for the sputtering. The rectifying diode and chip capacitor were then successfully soldered onto the microprocessed wafer. The characterization milestone was minimally achieved, since only microwave radiation absorption measurements with varying frequency and power were conducted. In addition, due to a lack of results during characterization, electrical characterization to determine power harvesting efficiency, as well as the demonstration of LED powering were not achieved. Since a power delivery to the load was unsuccessfully measured, the characterization milestone was not achieved based on the 10 µW acceptance criteria. The Reports milestone comprised of the interim report submission, as well as the submission for this final report. The interim report was submitted by the given deadline and contained a comprehensive outline of the design at the time. This final report will proceed in a similar fashion and will build on the interim report by presenting any deviations associated with the project. For the Symposium, the necessary information was compiled and processed for the presentation, and the poster was printed. The fabricated device was showcased; however, the LED demonstration was not achieved since the power transfer was not successfully verified in time.

4 Customer Requirements

A WPT system for implantable medical devices must satisfy a number of customer requirements to be an effective alternative to battery technology. The primary customer served by this project would be manufacturers of powered biomedical devices. The project also aims to meet the needs of the end-users, who are the patients receiving the implantable devices. In order to satisfy the requirements of the manufacturer, the device must easily integrate into current implantable devices, in terms of both power and geometry. The powering system must comply with regulatory standards of the United States Food and Drug Administration for medical devices. The system should also be relatively low in cost so as to not significantly increase the overall cost of the device, which is important for both the device manufacturer and the patient. More detailed customer requirements are shown in *Appendix A*.

5 Functional Specifications

In order to satisfy the customer requirements, a set of functional specifications for the receiving unit's design was generated. The objectives, their relative weighting, and their target values are outlined in further detail in *Appendix C*.

The primary functional specifications are derived from the principal customer requirements of safety and comfort for the patient. Thus, the main functional specifications are that the device design is small and lightweight (25% volume reduction compared to standard battery technology) and that it operates at low power (< 0.8 W). A small size is critical for integration of the receiving unit into implantable devices that are non-intrusive and not detectable to the patient. Since the power transfer mechanism involves microwave radiation, exposure safety considerations impose an upper limit on the power at which the device may operate. This maximum operational power was determined from the Consumer and Clinical Radiation Protection Bureau (CCRPB). There must also be sufficient power delivered to the load for proper operation. Given the safe power transmission limit, this consideration places a lower bound on the efficiency (> 10%) at which our rectenna system may operate.

The secondary functional specifications are that the rectenna should operate at an adequately large distance from the source (> 1 m), and the power transfer efficiency must not depend strongly on the incident angle of the microwave radiation. Additional specifications include long operational lifetime (> 10 years) and low cost.

Throughout the course of the project, it was found that many of the functional specifications were difficult to achieve with the time and resources available. Therefore, changes in design specifications were made, which were accompanied by a concentrated focus on the primary functional specifications, especially the small size and low power requirements. These changes in the design specifications are outlined in the following section.

6 Design Specifications

Design specifications were formulated based on the functional specifications. An initial design was proposed that was expected to satisfy the given functional specifications, however, it was found to be difficult to fabricate using the available microfabrication techniques. Fabrication complexities of the initial design led to the decision to pursue a different design. The scope of this project was limited by the time and facilities available.

The initial design consisted of an array of antennas connected through a feeding network to a rectification circuit that rectifies the signal captured by the antenna array. The array design allowed for high efficiency operation, due to the presence of many antenna elements. This specific design also had the advantage of operating properly for multiple incident polarizations, which helps to satisfy the low directionality functional specification. This design involved patterning on multiple planes. It was comprised of a layer of antenna array elements and a separate feeding network layer, which were connected using via through-holes, which are conductive connections between these different layers. The existence of vias represented the complexities in the proposed microfabrication procedures. An attempt was made to planarize the design by placing the feeding network on the same plane as the antenna array. However, the array's operation relies heavily on the coupling of the individual antenna arrays with each other and increasing the spacing between elements was found through simulations to diminish the efficiency of the device. Further details of the initial design are given in *Appendix F*.

The final design proposed is comparatively simple as it is contained within a single plane. In the interest of simplicity, single antenna elements were designed rather than attempting to couple a large array of antennas. Attaching single antennas to a rectification circuit is relatively simple. However, this simplified design cannot achieve the same power conversion efficiency, low directionality, and low polarization dependence achieved in the initial design. In this case, fabrication simplicity is a tradeoff with efficiency and directionality of the rectenna.

In the new design, a planar configuration was chosen due to its relatively simple simulation, fabrication, and integration into implantable medical devices (since a reduction in volume is one of our primary functional specifications). The components of the overall powering system were chosen such that they were small enough to fit the customer requirement outlined at the beginning of the report - this includes the antenna, rectifying diode, filter capacitors, and feeding network. Moreover, the interconnections and dimensions of the system must allow for impedance matching between the components, since a lack of matching leads to lower efficiencies through increased power loss. Finally, a target operation frequency of 12 GHz was chosen since the microwaves at that range have demonstrated the ability to penetrate and propagate through biological tissue. This chosen frequency is important for the design since the corresponding microwave length governs the dimensions of the antenna, and consequently, the rectenna system.

This design was based on the work by Tu et al [8]. The stepped- impedance dipole antenna used in this design allowed for a size reduction of about 23% as compared to conventional dipole antennas, which is desirable for the small size requirement for this device. The planar design bypassed multilayered complexity and allowed it to be fabricated with standard microfabrication techniques. The targeted frequency of operation for this design was 5.8 GHz. For further size reduction, the design intends to increase the operation frequency to 12 GHz, since that would enable scale down of the device dimensions. Through a literature search, 12 GHz was the highest frequency found that was able to effectively propagate through biological tissue [7]. The diode (MA4E1316 Schottky barrier diode) and

capacitor (2.4 pF chip capacitor) were specified by Tu et al. Finally, aluminum was chosen as the metal layer for the device due to affordability and availability.

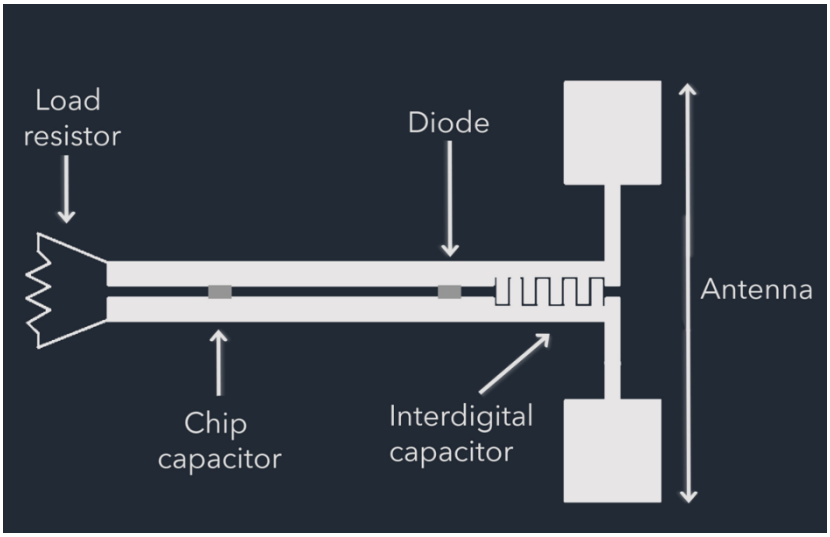

Figure 6-1: Design schematic from [8]

7 Verification Plan

A plan to verify the device design was prepared for tandem simulations of the antenna in COMSOL and rectification circuitry in Advanced Design System (ADS). The verification plan is unchanged from the previous design, and is detailed in *Appendix D*.

8 Testing Plan

A testing plan for validating the prototype was generated that involves generating a microwave signal through a signal generator connected to a horn antenna, and measurement of DC voltage for optimization of frequency, input power and load resistance. This plan was unchanged from the previous design, and is detailed in *Appendix E*.

9 Verification Data

Simulation Setup

A square slab of 500 µm thickness was used as the substrate, and was assigned either the Duroid 5870, for reproducing work in [8], or silica, for the design to be fabricated. On the top surface of this substrate, the 2-D features of the antenna (Figure 9-1) were mapped onto a work plane, which was assigned a perfect electric conductor (PEC) boundary condition (Figure 9-2a). This is a 2-D sheet of material with zero resistance and thus closely approximates the behavior of a thin layer of metallic material.

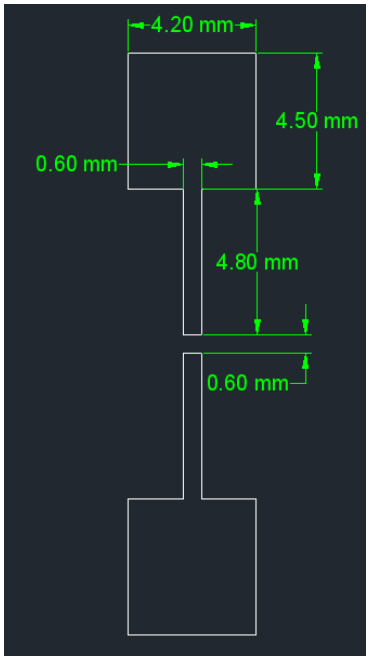

Figure 9-1: Antenna dimensions

The geometry was surrounded by an air box with perfectly matched layer (PML) boundary conditions (Figure 9-2b). A PML is an artificial absorbing layer for wave equations that is used to truncate the computational region without creating reflections off the boundaries. A lumped port boundary condition was placed in the gap between the dipoles to act as the source for wave excitation (Figure 9-2c).

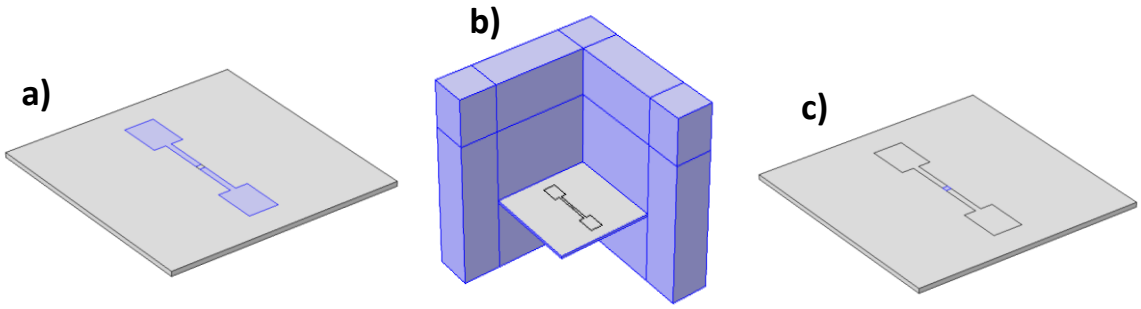

Figure 9-2: Boundary conditions in the COMSOL antenna simulations

The frequency-dependent impedance values of the antenna obtained via COMSOL were subsequently input into ADS, which was used to simulate the rectification components. The frequency-dependent impedance of the isolated antenna was input into ADS via a Data Access Component (DAC). The antenna was represented as an AC source port with frequency-dependent impedance using the values imported from COMSOL, while the coplanar striplines (CPS) were modelled as parallel microstrip lines. The rectification circuit was modelled as a set of lumped element components based on the design being reproduced. The interdigital capacitor, rectifying diode and chip capacitor components were included, and their respective parameters specified. The transmission lines were optimized to determine the placement of the diode and chip capacitor components for each simulation based on the best impedance matching. The load resistance was chosen as a standard 50 ohms for compatibility with standard testing equipment. A power probe was included to measure power dissipated across the load resistor. The ADS simulation schematic, including parameters of the lumped elements, is shown in Figure 9-3.

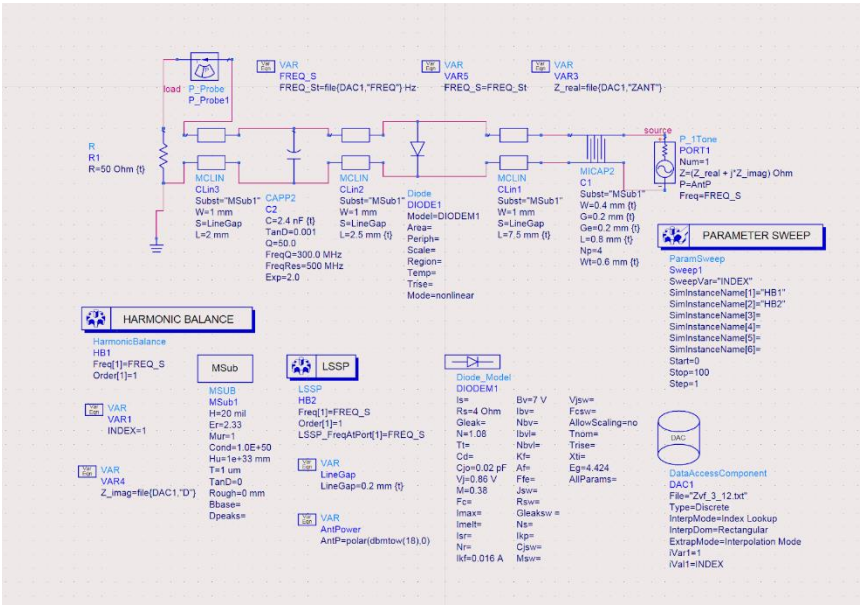

Figure 9-3: ADS schematic for the rectification circuit

Simulation Results

The antenna outlined in [8] was simulated in transmitting mode in COMSOL. The antenna was placed on the Duroid 5870 substrate that was used in the paper's simulations. From its feedpoint at the center of the two dipole arms, a wave excitation port transmitted a signal of various frequencies. By transmitting radiation from the antenna and performing calculations on the radiated electromagnetic field, the resonant frequency and the input impedance into the antenna were determined. The resonant frequency was determined to be the frequency corresponding to the minimum value of the frequency-dependent S_{11} (reflection coefficient) plot, where Port 1 was the excitation port placed at the feed point of the antenna (Figure 9-4a). The S_{11} values were also used to determine the input impedance of the antenna feedpoint (Figure 9-4b) . Details on these simulations are given in *Appendix D*. The results of these COMSOL antenna simulations are shown in Figure 9-4, while the corresponding impedance plots from [8] are found in Figure 9-5.

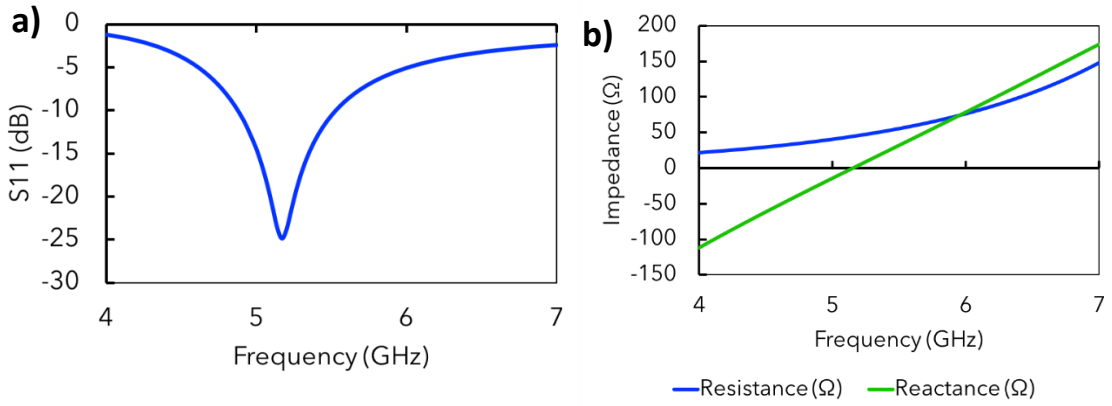

Figure 9-4: COMSOL antenna simulation on Duroid substrate; a) S11 vs Frequency and b) Impedance vs Frequency plots

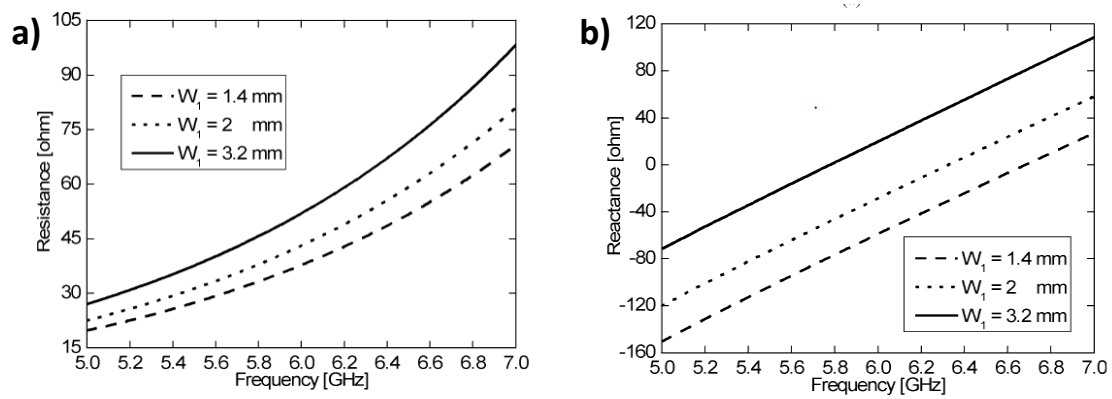

Figure 9-5: a) Resistance vs Frequency and b) Reactance vs Frequency plots presented in [8] for the antenna design

The results were similar to those shown in [8] with slight variations in the peak absorption frequency and the impedance values. The absorption peak was observed at approximately 5.2 GHz instead of the expected 5.8 GHz. This can be partially attributed to the inherent differences between the simulation softwares used, since Tu et al. used IE3D while COMSOL was used for reproducing their results. Since different software implementations solve equations in different ways, there can be discrepancies in the resultant solutions, even with the same geometries and boundary conditions in place. For example, in this case, IE3D uses the method of moments to solve electromagnetic wave equations, while COMSOL uses the finite-element method. Aside from this, given that the results of the paper are several years old, it is possible that simulation capabilities have increased, and that the results from the paper are slightly outdated, and potentially slightly inaccurate. While the general trend and approximate values of the resistance and reactance plots obtained are fairly similar, the reactance of the antenna appears to be shifted down in frequency by about 0.6 GHz, which corresponds with the mismatch in peak absorption frequency.

Next, the rectification circuit was simulated in ADS using the frequency-dependent impedance values obtained in COMSOL (Figure 9-4b). First, in order optimize the input power for the system, a power-sweep was performed (Figure 9-6). From this analysis, a power of 18 dBm (63 mW) was chosen for subsequent ADS simulations. Above 18 dBm, the maximum current of the diode was exceeded, and simulations failed to run.

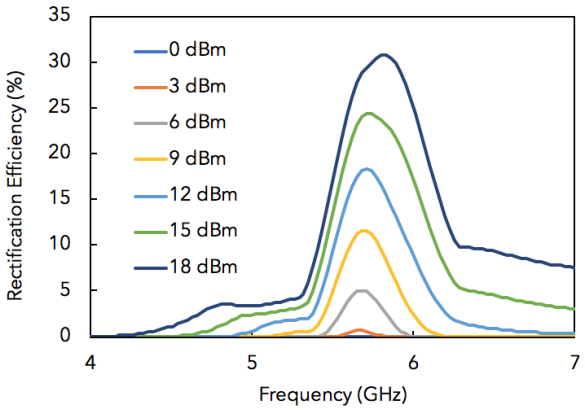

Figure 9-6: Rectification efficiency response to incident power sweep

Using the impedance values from the Duroid substrate COMSOL simulations, the rectification circuitry was characterized. The placement of the diode and chip capacitor measured from the interdigital capacitor was found to be 7.5 mm and 10 mm, respectively, based on the transmission line optimization for impedance matching. The frequency-dependent plot of the S_{11} parameter (Figure 9-7a) demonstrates a minimum reflectance peak at 5.8 GHz, which indicates that the circuit design is correctly optimized for the frequency of interest. The frequency-dependent plot of the rectification efficiency, which measures the power dissipated over the load as a percentage of input power, demonstrates a maximum efficiency of approximately 32% at 5.8 GHz (Figure 9-7b). This efficiency is significantly lower than the value reported by Tu et al. of 76% [8]. This discrepancy can be attributed to a lack of impedance matching between all the components of the circuit, including the diode, capacitors, and the transmission lines. Although reference [8] specified dimensions for the stepped-dipole antenna were given, dimensions for the CPS and the relative placement of the discrete components were not given, and it is therefore likely that the configuration that was simulated is not optimally impedance matched. This lack of matching would directly contribute to power loss along the rectification process, lowering the rectification efficiency of the system.

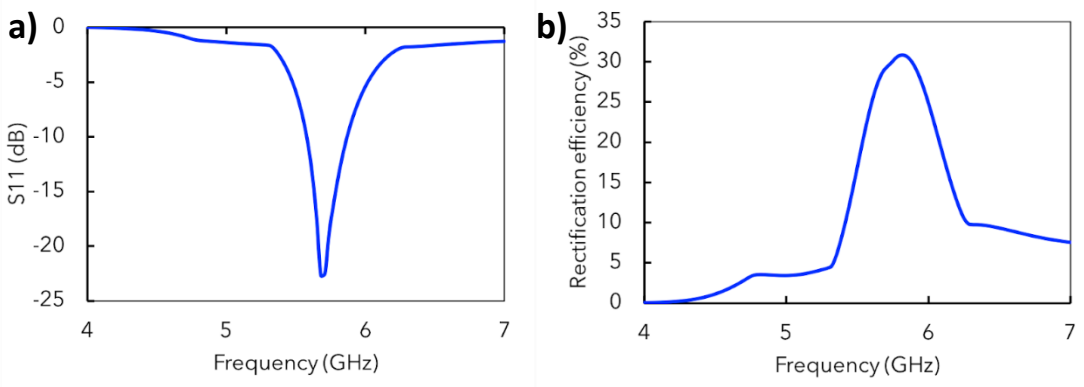

Figure 9-7: ADS rectification circuit simulation on Duroid substrate; a) S11 vs Frequency and b) Rectification Efficiency vs Frequency plots

Since a cleanroom microfabrication process was planned for the fabrication of the device, the simulations were performed again with a 500 µm thick silica substrate instead of duroid. Silica would be used during fabrication instead of Duroid due to its compatibility with photolithography. The results of this simulation are shown in Figure 9-8.

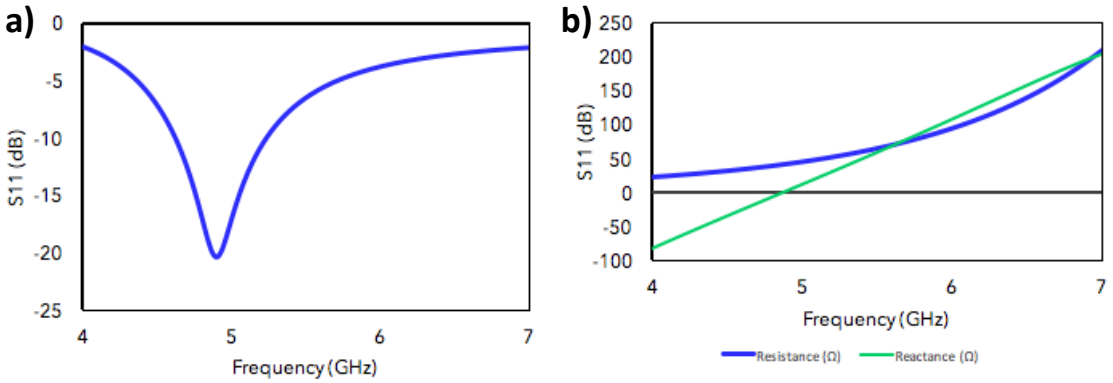

Figure 9-8: COMSOL antenna simulation on silica substrate; a) S11 vs Frequency and b) Impedance vs Frequency plots

These results show a shift of the peak of the S_{11} absorption and impedance plots of about 0.3 GHz lower in frequency. The new peak was observed to be at about 4.9 GHz. These results can be explained by the higher dielectric constant of the substrate, which led to a slightly higher impedance at all frequencies, and a different peak absorption frequency.

ADS was used to simulate the rectification circuit on a silica substrate. The antenna was once more modelled as a frequency dependent source in ADS with all components placed on a silica substrate. The placement of the diode and chip capacitor from the end of the interdigital capacitor was found to be 3.5 mm and 6 mm, respectively, based on the transmission line optimization for impedance matching. These simulation results are shown in Figure 9-9. Again, the frequency-dependent plot of the S_{11} parameter (Figure 9-9a) demonstrates a minimum reflectance peak at 5.8 GHz, once again confirming that the circuit design is correctly optimized for the frequency of interest. The frequency-dependent plot of the rectification efficiency demonstrates a maximum efficiency of about 35% at 5.8 GHz (Figure 9-9b), which is comparable to the value obtained for the Duroid substrate. This demonstrates that the effect of changing the substrate had little effect on the rectification efficiency, which was expected since the difference in permittivity constants between Duroid and silica is relatively small (2.33 vs. 3.58) [11].

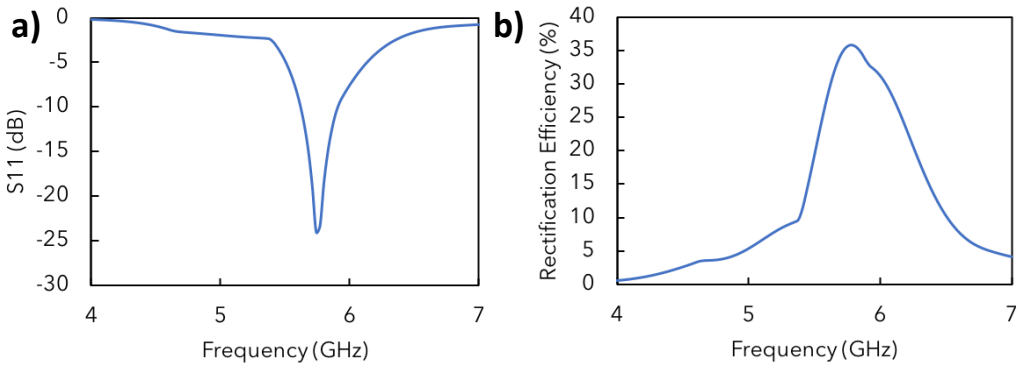

Figure 9-9: ADS rectification circuit simulation on silica substrate; a) S11 vs Frequency and b) Rectification Efficiency vs Frequency plots

Following this, the design was scaled down for 12 GHz operation, and analogous simulations were conducted. The COMSOL results are shown in Figure 9-10 and the ADS results are shown in Figure 9-11. Figure 9-10a clearly demonstrates a minimum reflectance peak at the target frequency of 12 GHz, while Figure 9-10b demonstrates similar trends for resistance and reactance as seen previously, with a

reactance of 0 Ω at 12 GHz. These results indicate that the scale-down of the antenna for operation at 12 GHz makes sense.

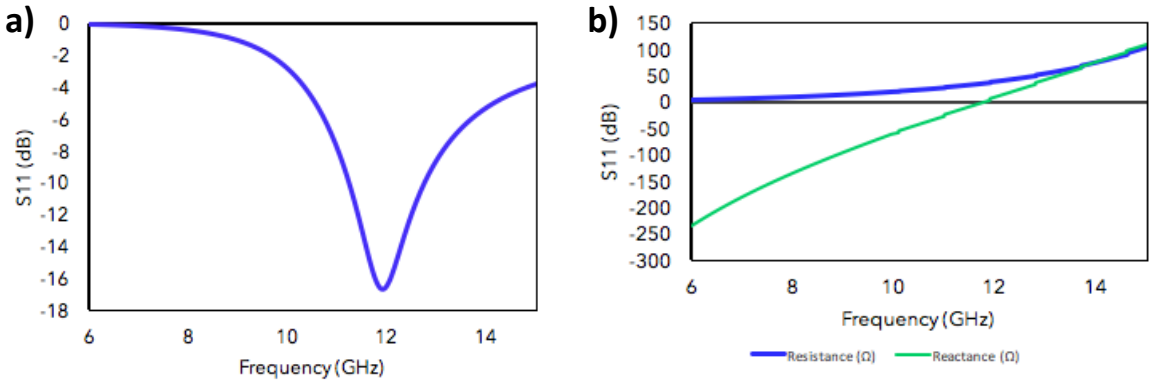

Figure 9-10: COMSOL scaled-down antenna simulation on silica substrate; a) S11 vs Frequency and b) Impedance vs Frequency plots

The rectification circuit was also scaled down in ADS. The placement of the diode and chip capacitor was found to be 2.5 mm and 9 mm, respectively, based on the transmission line optimization for impedance matching. Figure 9-11a demonstrates a minimum reflectance peak at 12 GHz, while Figure 9-11b shows a preliminary simulation of the rectification circuit, demonstrating a rectification efficiency of ~15% at 12 GHz. While these results do demonstrate that the scale down of the design is theoretically possible, the rectification efficiency is significantly reduced. This can be attributed to a lack of impedance matching once again, which is likely amplified in the scaled-down version due to the fact that the dimensions were not fully optimized, and the same discrete components were used as those used in the larger version of the simulation. Further improvements can thus be made by further optimizing the impedance matching and by finding discrete components that operate better in this new frequency range.

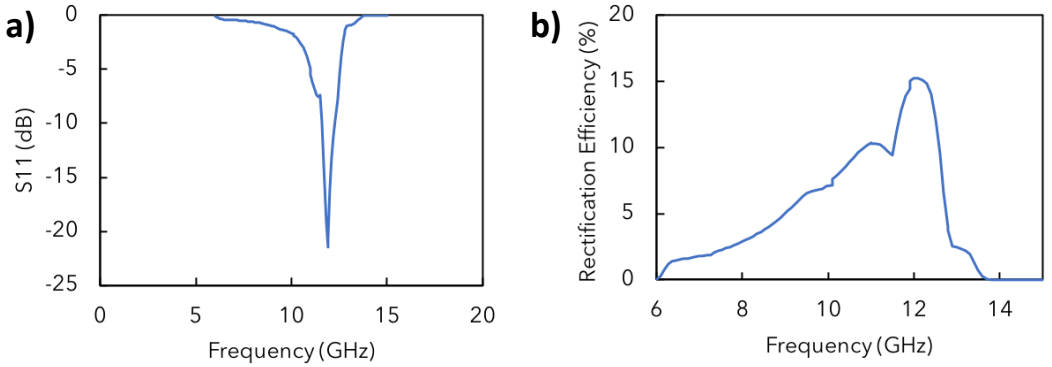

Figure 9-11: ADS scaled-down rectification circuit simulation on silica substrate; a) S11 vs Frequency and b) Rectification Efficiency vs Frequency plots

Overall, the verification data in the power sweep in Figure 9-6 shows significant rectification efficiencies at low power, which shows promise that the rectenna will satisfy the low power functional specification. Also, the antenna and rectification scale down results shown in Figure 9-10 and 9-11 show promise that the device will be able to be fabricated for 12 GHz operation, showing promise that the small size functional specification. Ultimately, the fulfillment of these functional specifications will need to be confirmed through characterization of the fabricated device.

10 Prototype Construction

Photolithography was chosen as the fabrication method to construct the prototype due to its advantages for fabrication of small feature sizes. Since the interdigital capacitor and diode have gap sizes of 200 µm, and the scaled down device will have even smaller dimensions, photolithography was necessary to achieve these feature sizes.

Step 1: Mask Design

A mask was designed to create the shape of the antenna using photolithography (Figure 10-1). The mask was created in AutoCAD modeling software. The mask was designed to be 4x4 inches so that it was compatible with the mask aligner in the undergraduate cleanroom. Four rectenna devices were created with varying stripline lengths and separation distances so that tuning of stripline impedance could be performed if testing results did not match simulation results. The top two designs have a wider stripline gap of 600 µm and the bottom two designs have a thinner stripline gap of 200 µm. The designs on the left side of the left have a stripline length of 20 mm while the designs on the right have a stripline length of 15 mm. A standalone antenna was also created for characterization of the antenna alone. Lines 100 µm in width were drawn between the devices as markings for laser cutting that would eventually be performed to separate the devices. All devices were designed to fit the diode and capacitor dimensions. For the larger stripline gaps, notches were placed in two possible locations for the diode attachment, based on simulations. This was due to the 200 µm width of the diode and capacitor being smaller than the larger gap size (600 µm).

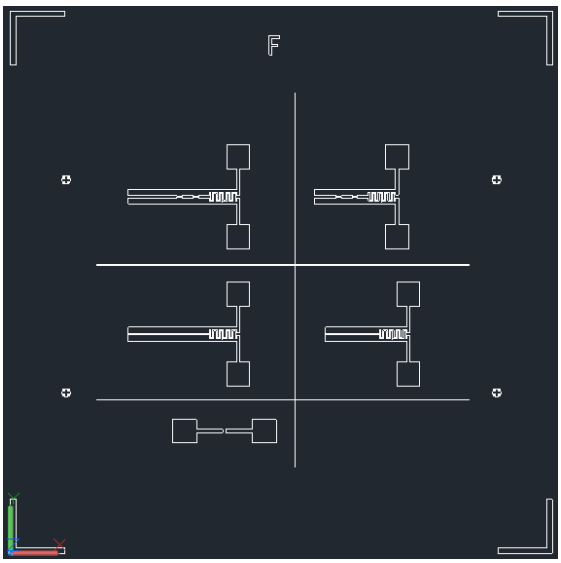

Figure 10-1: Mask design for fabricated rectenna devices

The dimensions of the design are shown in more detail in Figure 10-2 below. This design contains fully optimized locations for the capacitor and diode. The device that was fabricated had dimensions at 8 mm and 12 mm spacing for the diode and capacitor respectively instead of the 7.5 mm and 2.5 mm shown below. This is due to further optimization of the design after the first iteration of fabrication.

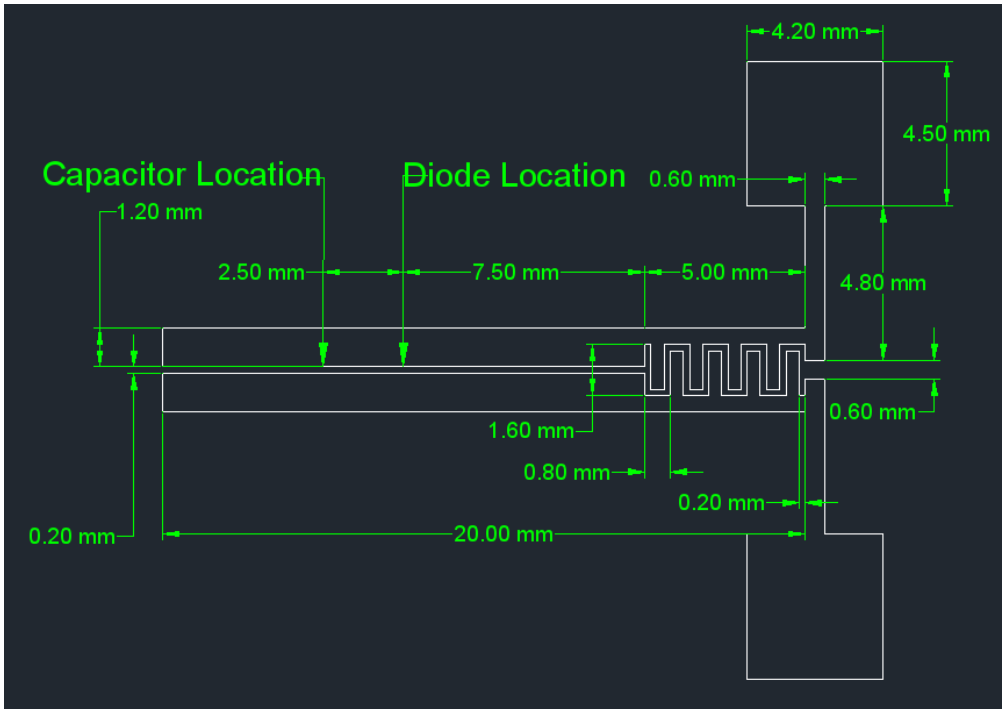

Figure 10-2: Dimensions of the fabricated antenna

After the mask was designed, it was purchased from mask supplier Front Range Photomask. The mask was printed with the data in chrome and the background in glass to accommodate a positive lithography process.

Step 2: Cleanroom Fabrication

To fabricate the device, the cleanroom procedure used in the NE455B laboratory was used. The process was fairly simple as only one structural layer was required. A schematic of the procedure is shown in Figure 10-3.

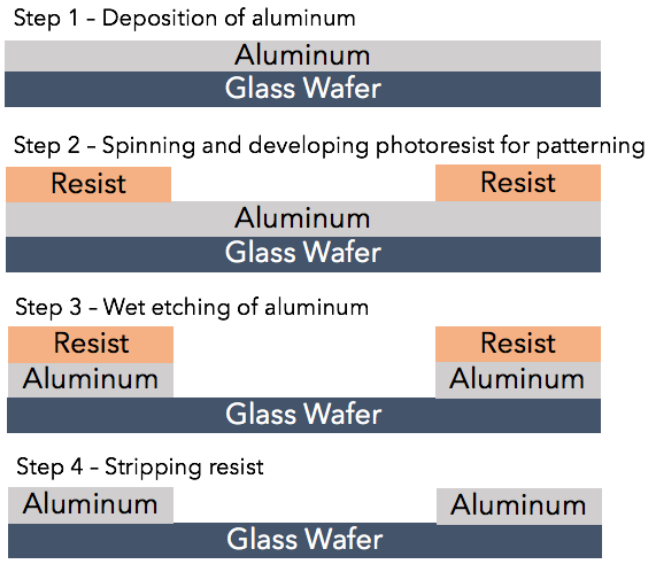

Figure 10-3: Microfabrication steps

Aluminum was first deposited on a glass wafer (glass was used as the substrate due to its relatively low dielectric in the 1-20 GHz frequency range, which was similar to Duroid [11]. The pattern of the device was then formed using photoresist. Finally, the device shape was etched into aluminum and the photoresist was stripped. A procedure outlining more details of the process is provided below [12].

1. Aluminum sputtering; Recipe = "NE455B_Al" (NOTE: This step was done in CIRFE as the sputterer in the undergraduate cleanroom was not working)
    a. Conditioning
        i. Power = 200 W
        ii. Time = 120 s
    b. Deposition
        i. Power = 500 W
        ii. Pressure = 3.5 mTorr
        iii. Flow Ar = 7.5 sccm, Temperature = 20 ºC, Time = 35 min
2. Photoresist Deposition
    a. Spin coat using Recipe 1 (3000 rpm)
    b. Bake wafer at 90 ºC for 5 minutes
3. Photoresist exposure
    a. Time = 5 s
4. Developing
    a. 45 seconds in developer solution (AZ 300 MIF Developer)
    b. Rinse with DI water
5. Post bake
    a. Bake wafer at 110 ºC for 5 minutes
6. Wet etching of aluminum
    a. Submerge in Aluminum Etchant Type A from Transene Company Inc. heated to 50 ºC until visible bubbling has stopped and pattern is clear
    b. Rinse with DI water for 5 minutes
7. Stripping photoresist
    a. Submerge in AZ KWIK Strip Remover for 3 minutes
    b. Rinse with DI water

Step 3: Discrete Component Soldering

After the device was fabricated and laser cut, the diode and capacitor components needed to be attached. The 2.4 nF capacitor was ordered from Digi-key (part number 490-1629-2-ND). The MA4E1316 Schottky barrier diode (manufactured by Macom) was donated by a local Macom supplier called Neutronics. This diode can also be found on Digi-key but only ships with a 100 unit minimum quantity (part number 1465-1024-ND).

Due to the very small component sizes, attachment methods were limited. Conventional soldering methods were infeasible since the solder would encapsulate the element itself, and the risk of shorting would be high. As a result, Bill Jolley, the ECE lab director from CIRFE was consulted for this task of attaching the components to the fabricated device. A 10-um tip was used to deposit a miniscule amount of EPO-TEK H20E Silver Epoxy onto the desired spots on both sides of the coplanar stripline, and the diode and capacitor components were carefully placed on top, as demonstrated below. The devices were then thermally cured in the oven for 1.5 hours to permanently solidify the silver epoxy, effectively "soldering"

the components to the device. The results of the final component attachments are shown in the device images in Figure 10-4.

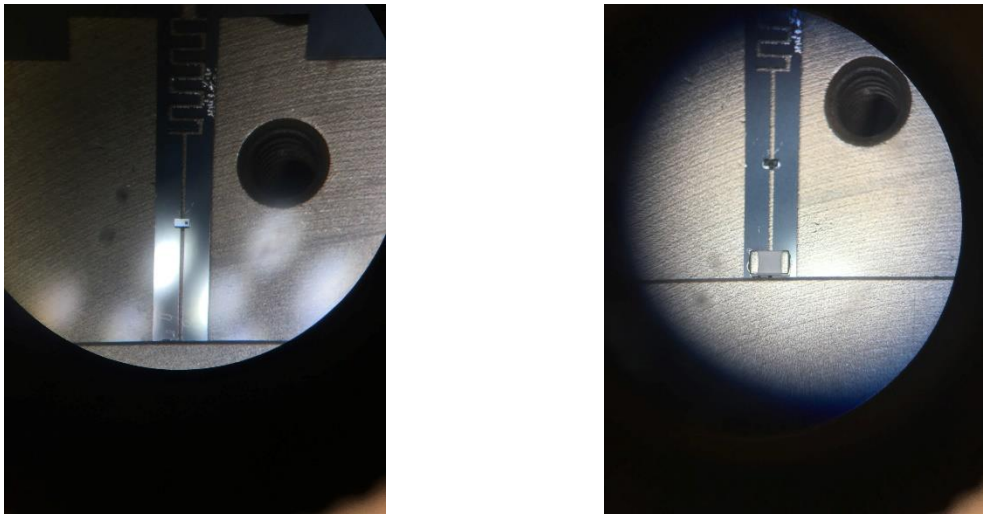

Figure 10-4: Component attachment, viewed through a microscope lens; a) diode; b) capacitor

11 Testing Results

Device measurements were performed by following the testing plan outlined in *Appendix E*. The results are documented in *Appendix H*. Evaluation of the connectivity of the metallic layer showed positive results, as a current could be measured between two spatially separated points on the rectenna, including across the soldered components. The connection between circuit components was tested, and their correct operation was also confirmed. Unfortunately, only steps 2 and 3 from the testing plan outlined in *Appendix E* were able to be performed. Step 1 was unable to be performed due to connection issues with the fabricated standalone antenna element due to the lack of a stripline. Steps 2 and 3 were performed but did not provide any measurable voltage for the rectenna system as a whole.

There are several reasons this may have occurred. Firstly, simulations were created assuming a certain input power incident on the fabricated antenna. In practical testing, however, the input power was specified based on the input power to the horn antenna from the signal generator. If there was significant loss in signal transmission from the signal generator, to the horn antenna, and finally to the fabricated antenna, the power reaching the fabricated antenna would be lower than assumed in simulations. However, this is unlikely since the rectification efficiency results at low powers outlined in Figure 9-5 of the *Verification Data* section shows rectification even at 3 dBm. The power loss from the horn antenna input to the diode input would need to be over 99.4% since horn antenna signals of up to 25 dBm were used and a rectification signal should be observed with a 3 dBm signal incident on the diode.

Another reason, albeit unlikely, for the lack of results could be faulty instrumentation in the experimental setup. A reference antenna of known characteristics (positive control) was not available for verification of whether the horn antenna and signal generator were operating correctly. Even though it is unlikely that instrumentation is the root cause of the issue, further validation of the experimental setup should be performed in order to rule out this failure mode.

A more likely source of the poor results is the lack of characterization of the antenna alone. Step 1 of the testing plan is very important as it allows for the individual characterization of the two components of the rectenna, the antenna and the rectification circuitry. Therefore, the next step for troubleshooting the device should be Step 1 of the characterization process. For this, a new antenna with a stripline to connect to an end launch connector for robust connection to a VNA should be fabricated in the next fabrication iteration.

12 Future Steps

The most immediate future step in this project is to ensure that the current testing setup is working. A number of problems exist which must be addressed. First, a reference antenna with known characteristics should be used to verify that the signal generator and horn antenna are performing as expected, and to measure the power that is being received by the rectenna in subsequent efficiency calculations. This calibration measurement should be performed prior to every validation measurement of any device.

Experimental characterization of the system would have been simplified if a coaxial connector had been added to the end of the CPS. This was not possible with the current design due to insufficient room for attaching this connector. Therefore, in subsequent fabrication runs, it is important that the CPS be sufficiently long to allow for the soldering of a coaxial connector to the edge of the substrate. These connectors would allow for the connection of a breadboard to the end of the CPS, where a matching network, load impedance, and/or various measurement instrumentation could be easily connected off-chip to the device.

Due to the integrated nature of the device design, it was difficult to troubleshoot and find the failure point of the device. In future iterations of fabrication, separate antennas, which are not connected to a rectification circuit, should also be included in the batch of devices, allowing for characterization of the standalone antenna. To easily probe the isolated antenna, there should be a short CPS to which a coaxial connector can be attached; this was not included in the current design. This standalone antenna would allow for the power transfer efficiency to be measured using a vector network analyzer (VNA). This would be achieved by connecting Port 1 of the VNA to the transmitting horn antenna and using it as a signal generator. Port 2 of the VNA would be connected to the feed point of the antenna through the coaxial connector. An S21 measurement (dividing the amplitude of the signal output from Port 1 by the signal input to Port 2), would help determine the power transfer efficiency of the system. Additionally, from this measured data, the frequency-dependent impedance of the antenna could then be calculated and verified against values determined by simulations. This calculation has been outlined in the context of simulations in *Appendix D*. This VNA measurement is also outlined as the first step in the testing plan in *Appendix E*; however, this could not be performed due to the aforementioned issues with the coaxial connector.

After characterization of the antenna is completed and it has been confirmed that the antenna has a sufficiently high efficiency, the full rectenna design with all of the components would be tested. If no DC voltage was measured across the load, then the design would need to be revisited, however this is unlikely due to the confirmation that the rectification circuit was operating correctly through simulations.

Assuming the verification of this proof of principle was successful, attempts to fabricate the rectenna on flexible substrates (such as Kapton tape preliminarily) could then be explored. Flexible substrates would allow for the rectenna to conform to surfaces, enabling implantable sensor manufacturers to place the rectenna on a passive surface of their devices, diminishing the volume required for a powering unit. Changing to a flexible substrate would require investigation of several potential challenges:

- The effect of changing the dielectric constant of the substrate
- The adhesion of the metal to the selected substrate material (may need to change the metal used depending on this)
- The effect on bending on the performance of the device, and whether or not this diminishes its performance (i.e. through fracturing)

In parallel, rectenna array designs should be investigated, as they are capable of more efficiently capturing incident microwave radiation due to the higher density of harvesting elements. Significant engineering challenges exist for rectenna array designs. For example, the placement of circuit elements is more difficult due to the dense packing of antenna elements. Moreover, arrays add complexity to the feeding network of the antennas due to their high packing density. In the first multi-planar design that was pursued (described in the *Design Specifications* section and in *Appendix F*), this issue was addressed by placing the feeding network on a separate plane and connecting the planes using vias. This, however, is not a viable option for this application due to the goal of having small devices that are low-cost, which requires relatively simple microfabrication processes. As such, in pursuing arrays of rectennas, having a uni-planar design is important.

Finally, given the promising results of the scaled-down simulations, the original goal of fabricating a high-efficiency 12 GHz rectenna should be pursued once the other complications have been addressed. Further simulations are required to find the device dimensions that optimize the impedance matching between components, thereby maximizing the total device efficiency. A new diode operating in the frequency range of interest, having an appropriate turn-on voltage, and dimensions that fit the device design would also need to be found. The same would apply for the chip capacitor.

Appendix A: Customer Requirements

The primary customers that this project aims to serve are patients that require implantable biosensors for proactive monitoring of their health. The project also serves doctors that prescribe the implanted device. The function of these implants is to proactively monitor the patient's relevant biological metrics to reveal problems before symptoms or complications arise. Several of these sensors have already been developed including a wireless small-intestine monitoring system to partly replace colonoscopies [13], a bladder pressure monitoring device for urological diseases [14], and a subdermal blood protein monitoring device for patients with chronic illnesses [15], to name a few. There are a multitude of implantable biosensors currently under development for treating a variety of conditions [16].

Safety

The implantable biosensor should be intrinsically safe. All materials used in the device should have no potential to harm the patient. The device should not increase risk of infection or any other complications. Power delivered to the device should be well controlled and should not cause heating of the device or the surrounding tissue so that tissue damage is avoided. Since far-field radiation is being used, the device should conform with radiation safety standards. In Canada, these standards are outlined by the Consumer and Clinical Radiation Protection Bureau (CCRPB) [6].

Regulatory Compliance

To be sold to patients in the United States, any medical device must be compliant with the United States Food and Drug Administration (FDA) medical device regulations. These regulations are found in CFR - Code of Federal Regulations Title 21 Parts 800-1299. FDA regulations are strict and comprehensive, requiring several costly and time-consuming steps [17]. In Canada, all medical devices must be compliant with Health Canada's Medical Device Regulations [18]. Since the scope of this project is only the development of a prototype powering system, this customer requirement is not as important of a consideration. Regulatory compliance becomes a significant concern only when the product is sold on the market. That being said, some regulations like the CCRPB radiation standards mentioned above are still important at this stage in the project due to their pertinence to the design of the power system.

Undetectable to Patient

To minimize the discomfort to the patient, the device should be effectively undetectable once it is inserted into the body. Ideally, there should be no lifestyle alterations due to the device. The patient should have full range of motion and no limits on their physical activity due to the device. The device should cause no pain and should have limited interaction with the body other than the specific system it is monitoring. The patient should not be required to think about providing power to the device or collecting telemetry that the device records. An automatic far-field powering system will significantly improve this aspect of patient experience.

Easy Implantation with Minimal Medical Intervention

To minimize discomfort to the patient, as well as complexity and time for the healthcare provider, it is crucial that the implanted device is introduced to the body using a fast and easy to perform process. Ideally, the medical implant should be administered through a small capsule or hypodermic needle depending on the location that the sensor must be placed. Any type of surgical procedure should be

avoided if possible. This introduces a requirement for the medical device footprint to be fairly small to accommodate the low-volume requirements of using a capsule or hypodermic needle as a vector.

Long Lifetime and Robustness

The implanted device should have a long lifetime to limit the need for surgical extraction and replacement of the device. A good standard to consider are pacemakers, which generally last about ten years (due to their battery life) [19]. The device should also be mechanically robust. It should be able to resist the stresses associated with remaining inside the body for long periods of time. Any repair or replacement would in many cases require surgical extraction, which is generally expensive and invasive. Long term power requirements are also an important aspect to consider, especially due to strict device size limitations and limitations on current battery technology. This is an area with a wireless power transfer system may be able to significantly improve device lifetime.

Low Cost

The implanted device should have a low overall cost to the patient or insurance company and healthcare provider. This cost is broken down into the cost of the device itself, the cost of the device implantation, and the cost of operation (telemetry tracking, powering and maintenance).

Appendix B: Project Plan and Milestones

Design and Simulations

Simulations will be conducted separately for the antenna and the rectifying diode. The RF module in COMSOL will be used to optimize the antenna parameters. Design parameters include metal selection for the antenna, as well as geometry that maximizes absorption of microwave radiation in the frequency of interest (~12 GHz) and achieves an impedance that can be matched by the rectification circuitry. A matching network, along with the diode, will be simulated using Advanced Design System (ADS). The software can be used to optimize dimensions of transmission lines for effective impedance matching of the antenna. A model of the diode can be implemented to select for optimal parameters. This can be incorporated with a model of a capacitor for low-pass filtering, and a resistor to act as the load. The power dissipation across the load can be used to determine the rectification efficiency of this system and optimize its parameters. Once diode parameters are determined, these characteristics can be applied to the antenna simulation. Subsequent iterations between antenna and diode simulations will be done to determine the optimal parameters for the system. The results of these simulations will define the fabrication specifications.

Assigned to: Adam, Graham, Kai, Nayera, Dhilan

Acceptance criteria: Achieve a design that is possible to fabricate and has a theoretical efficiency of greater than or equal to 10%.

Deadline: December 4, 2017

Material Acquisition

Appropriate suppliers will be contacted, and lowest cost suppliers will be selected.

Assigned to: Adam, Dhilan

Acceptance criteria: Materials have been acquired within the project budget.

Depends on: Simulations and design completed

Deadline: January 12, 2018

Fabrication

In parallel with simulations and design optimization, access and training for fabrication facilities will be obtained. Fabrication is expected to consist of photolithography, metal sputter coating of copper, and lift-off processing. External flip-chip components including the rectifying Schottky diode and the load resistor will be soldered on after microprocessing has been completed.

Assigned to: Nayera, Adam, Graham

Acceptance criteria: Device has been successfully fabricated and prepared for characterization.

Depends on: Simulations and design completed and materials acquired.

Deadline: January 19, 2018

Characterization

For the purpose of validation, characterization will be performed inline with fabrication. Following fabrication, additional characterization will be performed in order to ensure that the devices meet the specified design and functional requirements. Fabrication validation will include scanning electron microscopy and electrical characterization using a probe station. Post-fabrication characterization includes anechoic chamber microwave radiation absorption measurements, electrical characterization to determine power harvesting efficiency, and demonstration of LED powering.

Assigned to: Graham, Kai, Nayera

Acceptance criteria: Device demonstrates the expected I-V characteristics and power delivery to a load of at least 10 µW.

Depends on: Device has been fabricated.

Deadline: February 9, 2018

Data Analysis

The experimental absorption, rectification and power efficiency of the fabricated devices will be measured. Results will be compared to literature, and this data will point towards further improvements that can be made to the product.

Assigned to: Kai, Dhilan

Acceptance criteria: Characterization data has been processed to yield device metrics that indicate device performance.

Depends on: Device fabricated and characterized.

Deadline: March 9, 2018

Reports

Results and progress will be documented throughout the process. The interim and final fourth year design project reports including all design decisions and project results will be completed.

Assigned to: Adam, Graham, Kai, Nayera, Dhilan

Acceptance criteria: Reports have been completed to fully outline the design and satisfy course requirements.

Depends on: Data analysis completed.

Deadlines:

- Interim Report: December 4, 2017
- Final Report: April 4, 2018

Symposium

The final fabricated design will act as a functional prototype for demonstration of the completed project at the 2018 Nanotechnology Engineering Symposium. Ideally, the prototype will demonstrate energy harvesting from a microwave radiation source to power a simple load, such as an LED.

Assigned to: Adam, Graham, Kai, Nayera, Dhilan

Acceptance criteria: Information compiled and poster printed.

Depends on: Data analysis completed.

Deadline: TBD

Human Resources

Table B-1: Human resources

Category	Nayera	Adam	Graham	Kai	Dhilan	Total
Simulations	**55**	**55**	**55**	**55**	**55**	**275**
Design and CAD	**45**	**45**	**50**	**45**	**45**	**230**
Fabrication	**20**	**15**	**20**	**10**	**10**	**75**
Optoelectronic characterization	**45**	**45**	**40**	**45**	**45**	**220**
Data Analysis	**35**	**35**	**35**	**40**	**40**	**185**
Report Writing	**10**	**15**	**10**	**15**	**15**	**65**
Total Hours	**210**	**210**	**210**	**210**	**210**	**1050**

Timeline

Table B-2: Timeline

4A

Week	1	2	3	4	5	6	7	8	9	10	11	12
Research							Midterm week					
Design												
Simulation												
Interim Report												

4B

Week	1	2	3	4	5	6	7	8	9	10	11	12
Material Acquisition											Symposium	End of term
Fabrication												
Characterization												
Data Analysis												
Report												
Symposium												

Appendix C: Functional Specifications

Safety

With any biomedical application, safety sets very high-priority constraints and requirements for design. The main safety considerations for this application are the maximum power that can be transmitted without causing harm to the patient, and the corrosion of the powering unit. Because WPT is the basis of device operation, it is critical that the required transmitted power be within the safety constraints for radiation at the design frequency of 12 GHz. Additionally, it is necessary that the device has a high enough efficiency such that it requires no more power than the upper power limit for safe radiation transmission in an uncontrolled environment.

According to the CCRPB, for radiation with frequencies in the range of 6 GHz to 15 GHz, power density serves as the exposure limit metric [6]. The maximum allowable electric field strength is $E_{RL} = 61.4\ V_{RMS}/m$, and the maximum allowable power density is $S_{RL} = 10\ W/m^2$. Both of these values are obtained over a reference time period of 6 minutes. In the case of indefinite exposure, which encompasses this application, the time average of the squared value of the electric field strength over any time period equal to the reference time period must not exceed E_{RL}^2. Similarly, for indefinite exposure, the time average of the power density over any time period equal to the reference period cannot exceed S_{RL} [6]. To be conservative with design constraints, the square of the electric field strength will be limited to $0.75E_{RL}^2$ and the power density to $0.75S_{RL}$. This yields a maximum electric field strength of 53 V_{RMS}/m and a maximum power density of 7.5 W/m^2.

Using a simple weight-based calculation for body surface area (BSA) of a child [20] and the average mass of a baby [21], we obtain a BSA of approximately 0.22 m^2. Using this value, the maximum safe transmitted power is found to be approximately 1.6 W. As safety is a top-priority requirement, a conservative approach is taken to determine the design constraints. Thus, the design constraint is set to half of the maximum value found using the regulatory limits, i.e. 0.8 W.

The transmission efficiency through biological tissue is around -51 dB (~0.28%) [7], meaning that assuming the maximum safe power of radiation is transmitted from the transmitting unit (0.8 W), the power at the input of the antenna would be approximately 2.24 mW. The power needed to drive the rectifier at the range of frequencies of interest is on the order of tens of microwatts [7]. To be conservative with the design constraints it is assumed that the power required at the rectifier is 100 µW. Using these values, the minimum absorption efficiency of the antenna allowing the device to operate within the maximum safe radiation power limit is found to be approximately 5%. Again, to be conservative, the design constraint will be limited to 10% efficiency.

With regards to corrosion prevention, biocompatible, medical-grade materials must be used in bio-implantable applications to ensure safety. Such materials are highly resistant to corrosion, preserving device integrity, reducing the risk of device failure, and preventing the dangerous implications of oxidation of materials inside biological tissue.

Comfort

Comfort is one of the most important requirements for any implantable biosensor or prosthesis. In the case of implantable biosensors, comfort is achieved primarily by having the smallest and most unobtrusive devices possible. Functionally, this requirement sets size and weight constraints on the implant, and thus on all of its individual components, including the powering unit.

Currently, typical capsule bio-implants have areas on the order of 0.75 cc [22]. Compatible batteries have an average volume of 0.14 cc [22], which is a substantial portion of the entire implant. The dimensions of the powering unit should be such that they eliminate much of the battery's volume inside the biosensor.

Robustness

In addition to safety, the corrosion resistance of the powering unit is important for a robust and long-lasting device. Implantable biosensors should be highly reliable devices with long lifetimes, lasting over 10 years. Additionally, the transmitting unit should be able to power the implanted device at reasonably large distances and at wide angles with the respect to the point of transmission. This ensures that the device does not require the wearer to be restricted to limited spaces when powering it.

Cost

In attempting to replace batteries in implantable biosensors, the price of the alternative powering unit ideally should not exceed that of the current technology. Due to the novelty of the technology, especially when compared with batteries due to their prevalence, the proposed alternative powering unit will likely initially exceed the price of current battery technologies. However, the increase in price must be reasonable enough to justify switching to the alternative technology. Due to the many other advantages of the rectenna powering unit, cost is relatively low in priority with regards to the other functional specifications.

Summary

Table C-1 summarizes the functional specifications, their target values, and their relative weight in importance.

Table C-1: Summary of functional specifications

Objective	Weight	Measurement or Estimation	Target
Small, lightweight	35%	Percent reduction of volume V in the biosensor allocated to the powering unit when compared to current battery technology's average size	V > 25%
Low power	25%	• Power P of radiation required to be transmitted from transmission unit to power device • Electric field F of radiation required to be transmitted from transmission unit to power device	P < 0.8 W F < 53 V_{RMS}/m
High efficiency	15%	Percentage E of total power transmitted from transmitting unit is absorbed by the antenna	E > 10%
Large distance	10%	Device is powered up to a separation distance D from the transmitting unit	D > 10 m
Low directionality	8%	Device is powered up to an angle A measured on either side of the front of the transmitting device	A > 60^o
Corrosion resistance	4%	Corrosion resistance R as a percentage of corrosion resistance of surgical stainless steel	R > 98%
Long lifetime (durable)	3%	Fully functional for Y years	Y > 10
Low cost	3%	Estimated price C as a percentage of average retail price of state-of-the-art batteries in implantable biosensors	C < 120%

Appendix D: Verification Plan for the Paper Design

Based on the work by Almoneef et al [23], a hybrid simulation approach involving two simulation softwares was used to verify and make modifications to existing designs based on the previously outlined functional specifications. In [23], the antenna was simulated in HFSS, which is a simulation software commonly used for RF systems, while the rectifying circuit of the rectenna was simulated in Advanced Design Systems (ADS). In this project, a similar approach was used, however COMSOL was used in place of HFSS for the antenna simulations. The rationale for this deviation was two-fold. One, familiarity with COMSOL was exploited in order to circumvent the technical and time challenges of learning a new software. Two, this alternative approach using COMSOL to corroborate standard HFSS results was successfully achieved for a previous design, demonstrating the validity of the alternative, and presenting an interesting pursuit.

More specifically, through simulation, after confirming the validity of the reproduced results, the design can be readily scaled down through parameterization, in order to verify that the size requirement can be met. The efficiency can be measured through the simulation by comparing the final power dissipated across the load with the input power of the system. By changing the input power of the simulation, the low power requirement can also be verified. Low directionality can in turn be verified by sweeping the incident angles of the microwave radiation and measuring the change in efficiency.

The antenna was first simulated in transmitting mode. Simulation in transmitting mode allows for the determination of the resonant frequency as well as the input impedance into the antenna. By transmitting radiation from the antenna and observing the radiated electromagnetic field, these properties can be determined. An antenna's resonant frequency is essentially the frequency of electromagnetic radiation at which it is best impedance matched to the ambient environment, allowing for the least reflection of the radiated field back toward the antenna. Hence, the resonant frequency is determined to be the frequency corresponding to the minimum value of a plot of S_{11} reflection as a function of frequency (where Port 1 is the excitation port placed in the feedpoint of the antenna from which the radiated field emanates).

The frequency dependent reflection plot (S_{11} vs frequency) is also used to determine the input impedance of the antenna feedpoint, which is a property critical for impedance matching the antenna to the rectification circuitry to maximize the power transfer efficiency between these components. The impedance Z is given by the following equation [24]:

$$Z = Z_{feed}\left(\frac{1 + S_{11}}{1 - S_{11}}\right)$$

where Z_{feed} is the reference impedance of the feedpoint of the antenna from which the transmitted waves emanate. The value of Z_{feed} was set to 50 Ω, although the value has no impact on the results, since the reflection coefficient S_{11} depends on this value.

The frequency dependent impedance was taken from COMSOL and imported into Advanced Design System (ADS) to model rectification circuitry. Components of rectification circuitry were modelled as lumped elements. The S_{11} parameter, representing reflection from the circuit, was evaluated to determine the optimal operation frequency. A power probe over the load resistor is used to determine rectification efficiency by comparison to input power.

Appendix E: Test Plan for the Constructed Prototype

Preliminary device testing includes probing to ensure that the electrical connections are robust. A digital multimeter (DMM) can be used to determine the continuity of the metal in each half of the antenna and the connections between device components. The next step is to verify the built-in voltage of the diode and the capacitor capacitance. The device measurements are performed in an anechoic chamber to isolate it from ambient radiation. The CPS is probed and connected to the DMM. A horn antenna is connected to a signal generator and a microwave signal is directed at the device.

The testing plan (Figure E1) is as follows:

1. The first step involves measurements of an isolated antenna, which includes only the stepped impedance dipole. This measurement is taken by connecting Port 1 of the VNA to the horn antenna as a signal generator and connecting Port 2 to the feed point of the antenna. Frequency is then to be swept and an S21 spectrum is captured by the VNA, which would subsequently used for antenna efficiency and impedance calculations. This spectrum also determines the resonant frequency.
2. Next, the entire device, including the rectifying circuit, can be evaluated. Setting the output signal from the signal generator to the previously determined resonant frequency, power can be swept to find the necessary power for device operation.
3. Subsequently, another frequency sweep can be performed at this power to fine-tune the frequency for optimal device performance and capture a spectrum at the optimal power of operation.
4. Finally, with the frequency set to the resonant frequency, and the power set to the operation power, the load resistance can be varied in looking for the maximum power, which indicates optimal impedance matching and therefore maximum dissipated power.

The separation distance between the source and device, as well as the angle of incidence of radiation, can also be varied to determine the effect of these parameters on device performance.

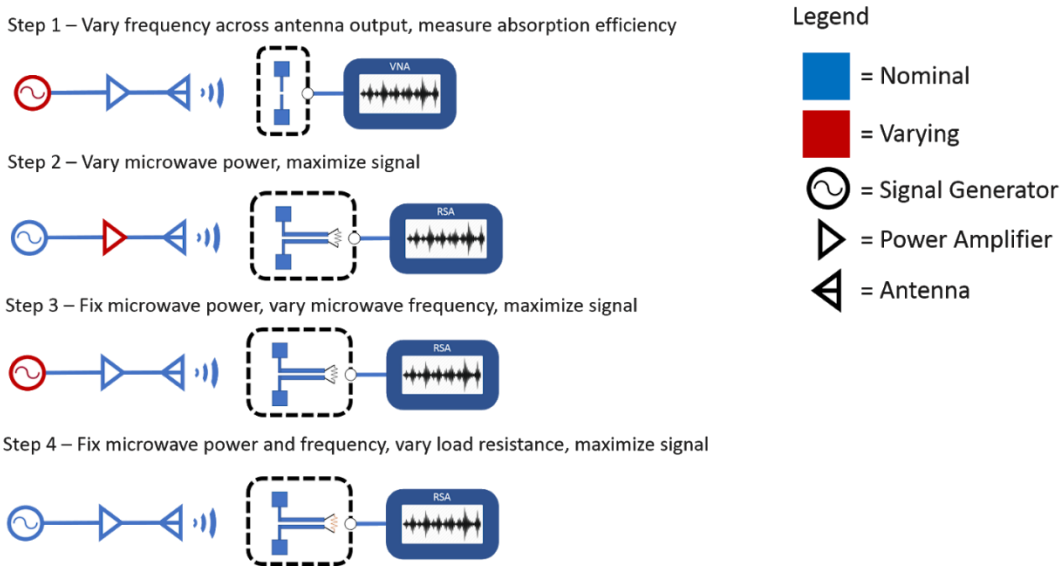

Figure E-1: Testing plan

Appendix F: Design Specifications

Background

The work of Almoneef et al. [23]serves as the basis for this design and presents a dual-polarized metasurface absorber operating at a frequency of 2.4 GHz. A metamaterial absorber works because its cells have a surface impedance that is matched to the impedance of free space, allowing for efficient power transfer to the absorber [23]. Impedance matching is achieved by tuning the effective relative permittivity and permeability of the metamaterial by modifying the geometry, resulting in its effective refractive index being matched to that of free space (i.e. n = 1) [23]. Energy harvesting applications require channeling of the captured energy to a load. In the presented design, the energy collected by the absorber is channeled to a feeding network that collects AC power and feeds it into a matching network, which is followed by rectification circuitry and the load.

The unique aspect of the presented design is the coupling of individual unit cells into "super cells". A super cell in this design consists of 16 individual unit cells arranged in a 4x4 array (Figure F1). A feeding network to which the absorbed power is to be channelled is in a layer below the metamaterial and is connected to the absorber through a via in each of the individual unit cells. The position of the via is alternated for adjacent cells, which allows for dual-polarization operation. This configuration allows for energy harvesting from various incident angles, increasing the absorption of the surface.

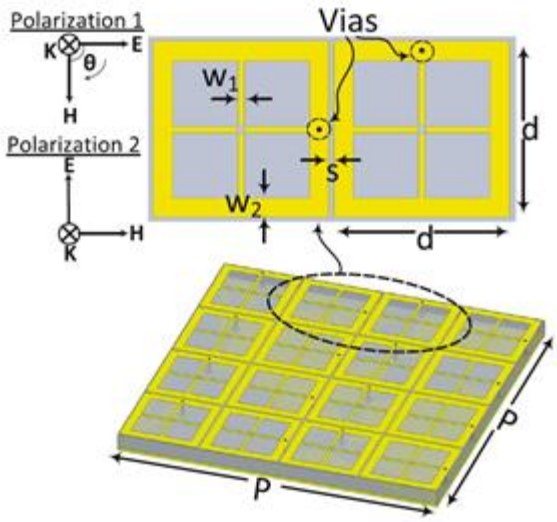

Figure F-1: Schematic showing the super cell of metamaterial absorber [23]

The metasurface is supported by a layer of dielectric material that is low-loss at the operating frequency. The dielectric layer is backed by a ground plane that reflects waves transmitted through to the metasurface and back towards the metamaterial, serving to increase absorption. Typically, perfect absorbers utilize lossy dielectric layers to capture and dissipate energy. For energy harvesting applications, this captured energy must also be channeled. For this reason, the dielectric material was selected to be low-loss at the operating frequency. Energy dissipation must be concentrated within the load rather than lost in the dielectric material in order to be useful as an energy harvester.

Grouping unit cells within a super cell has the advantage of reducing the number of required feeding ports. This particular super cell layout consists of 16 unit cells, 8 of which capture waves of one polarization and the other 8 of which capture waves of the orthogonal polarization. All 16 cells of a single super cell can therefore be fed with only two feeding networks, one for each polarization. Thus, the channeling network to the rectifying circuitry (Figure F2) is greatly simplified. This maximizes the efficiency of the power transfer from the absorber to the rectifying circuitry as the number of somewhat lossy copper traces is reduced.

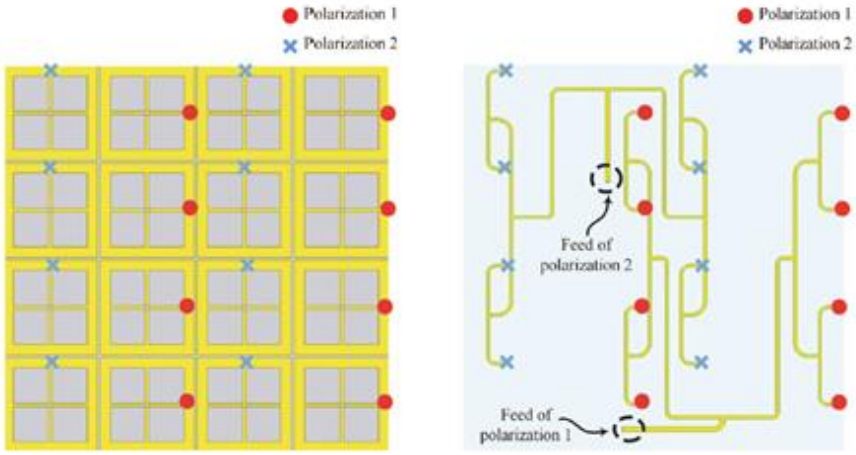

Figure F-2: Schematic showing the feeding network (right) and the locations of the connecting vias on the metasurface (left) [23]

The unit cells are strongly coupled, which allows for absorption and efficiency values close to unity even though only half of the unit cells absorb the energy for a given polarization. This can be seen in Figure F3, where for a given polarization, the absorbed power is concentrated in the unit cells for which the via is contained in the arm perpendicular to the electric field vector. If the unit cells were weakly coupled with each other, maximum theoretical efficiency for a given polarization would be limited to 50%.

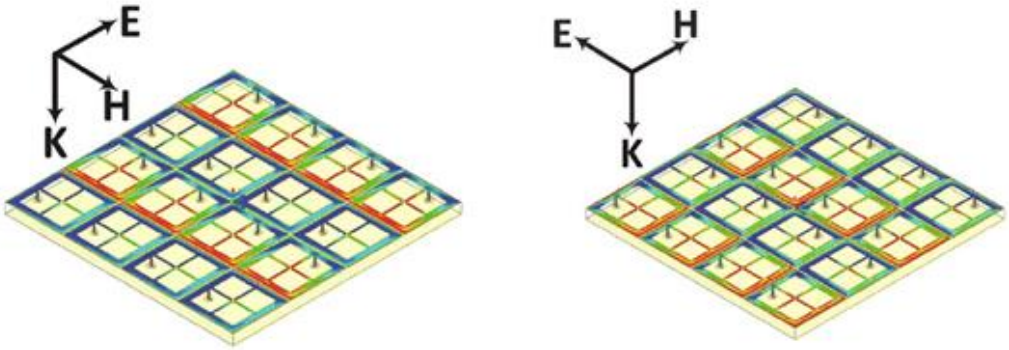

Figure F-3: Electric field magnitude surface plot of the metamaterial super cell for different orthogonal polarizations [23]

Some designs channel all the collected AC power to a single rectification network (i.e. AC channeling network), while others have a rectifier for each individual element (i.e. DC channeling network) [23]. In AC channeling networks, AC losses can be significant, especially in the case of networks with large footprints. DC channeling networks can also introduce losses due to the increased number of diodes. The presented channeling mechanism makes use of both AC and DC channeling networks. The AC power collected by 8 cells for each polarization is combined to one single feed (i.e. AC channeling), and each of these feeds is connected to its own rectifying element (i.e. DC channeling). In addition to simplifying the

feeding network, this configuration further improves power transfer efficiency by reducing the number of diodes necessary. With this feeding network configuration, only 2 diodes are needed per super cell, as opposed to all 16 constituent unit cells requiring a diode. Since AC to DC conversion losses increase linearly with the number of diodes, this significant reduction in the number of diodes necessary drastically improves the AC to DC conversion efficiency. It also reduces the cost, due to fewer diodes required.

In the presented design, the feeding network is on a different plane than the metamaterial absorber. This reduces the lateral footprint of the entire system. The feeding network is supported by its own layer of dielectric material, which is attached to the bottom of the ground plane. This forms three "active" layers – the metamaterial absorber, the ground plane, and the feeding network – with dielectric layers in between. The ground plane is thus sandwiched between the metasurface and the feeding network, which are connected to each other through vias. An exploded view of the stacked structure is shown in Figure F4.

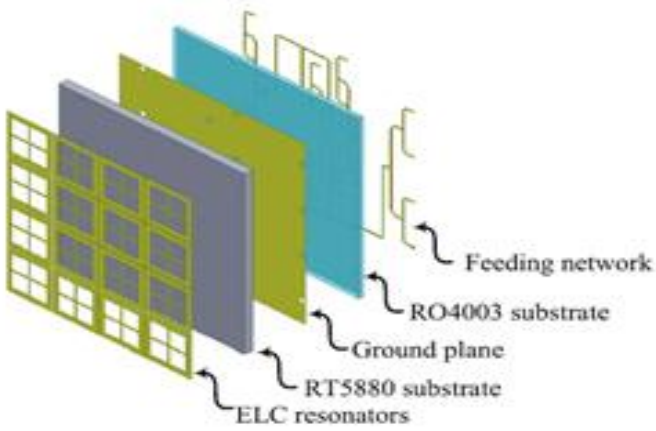

Figure F-4: Exploded-view of device layers

The simulated efficiency of the presented design was high, with the radiation to AC conversion efficiency found to be approximately 90% using HFSS, and the AC to DC conversion efficiency found to be approximately 80% using ADS. The simulated design was fabricated to verify the calculated efficiencies with experimental results. A 3x3 array of super cells was fabricated and was shown to have 70% overall efficiency.

Antenna Array Project Design

The chosen design for remotely powering implantable biosensors involves an array of microfabricated metamaterial antennas connected through a feeding network to a matching network and a Schottky diode, which rectifies the received signal. The metamaterial platform allows for a significant size reduction in the powering unit of implantable sensors as it provides a thin, planar design which can be implemented on the existing non-functional surfaces of the sensor as an alternative to the bulky design of current batteries. Thus, the metamaterial design effectively eliminates the volume of the battery inside the devices, thereby satisfying the requirement for a small design.

The power efficiency of the powering unit is another important functional specification. The main factor in determining the total efficiency of the rectenna is the antenna absorption efficiency. Consequently, the antenna design is a critical aspect of this project. The proposed design consists of a metamaterial absorber array with cross-hair-shaped unit cells as the receiver of 12 GHz microwave radiation.

This particular design was selected since an implementation of this design with a longer wavelength has been achieved in the project consultant's laboratory, with an operating frequency of approximately 2.4 GHz [23]. Additionally, this design consists of arrays of strongly coupled unit cells, forming super cells, which are designed to absorb waves of multiple polarizations, reducing the directional restrictions of the absorber. The super cells also have the advantage that they allow for a more optimized feeding network configuration, which improves the radiation to AC conversion efficiency. An operating frequency of 12 GHz has been selected as the operating frequency for this application, as this frequency has been found to be optimal for power transfer efficiency through biological tissue [7].

Functional specifications require that the total device size be on the order of an implantable biosensor. This requirement is satisfied by choosing to use a planar design, such as the metamaterial absorber array described above. Scaling down the cross-hair design described in [23] to the desired operating frequency of 12 GHz leads to super cell dimensions of approximately 13.5 mm by 13.5 mm. These dimensions were verified through simulations, resulting in an antenna that preferentially absorbs at 12 GHz (see *Appendix G*). In order to have an effectively large array size, the design will start with a 2x2 array of super cells, which leads to a total size of approximately 3 cm x 3 cm in area. Given these target dimensions, microfabrication is the appropriate technique to fabricate the rectifying antenna circuit components, since dimensions as small as 20 μm are achievable by conventional photolithography.

In designing a rectenna, low-pass frequency filters are typically used to remove higher order harmonics which may be generated by the antenna or the nonlinear response of the diode. Failure to remove these higher order harmonics decreases the overall system efficiency. To circumvent this efficiency reduction, Sun et al [25] designed the antenna such that the Schottky diode is impedance matched with the antenna at the frequency of operation and mismatched for all other frequencies [25]. Thus, power is only delivered to the diode at the desired frequency, and the need for a low-pass filter is eliminated. The proposed design attempts to mimic this design choice by designing the antenna metamaterial to have a matched impedance with the rectifying circuitry only at the frequency of operation.

To meet the functional requirement of safety in an implantable biosensor, this device will operate at low power to minimize the risk of electrical shocks and tissue heating. Ideally, the power conversion efficiency should be as high as possible, thereby requiring lower power transmission to rectify a signal. Efficiencies up to 90% [26] are frequently achieved in GHz frequency rectifying antenna devices. Since power efficiency is not a critical figure of merit in this low power application, a power conversion efficiency of greater than 10% will be considered acceptable, since it allows for operation within the safe maximum power constraints.

A conventional off-the-shelf Schottky diode, such as an HSMS-2852 (used in [23]), will be used to rectify the signal captured by the antenna. The use of a Schottky diode is necessary in this high frequency (GHz) application since the switching times of pn-junction diodes are not short enough for correct operation at these frequencies. The diode will be soldered to connect to the matching network on the silicon wafer after the antenna has been fabricated, and a resistive load will be connected following the diode. For the purposes of demonstration, the load over which the power received will be dissipated will be an LED. Initial measurements will be performed using a load resistor, for the purposes of simplicity and characterization. While the goal of this technology is to power micro-sized implantable biosensors with stringent size requirements, this demonstration of powering an LED will act as a proof of principle. Following the completion of this stage of the project, an oscillator circuit and a power amplifier may be designed and fabricated for the transmitting aspect of the project, if time permits.

Fabrication

Since unit cell dimensions are on the low end of the millimeter scale, the system has critical features that are smaller than the minimum machinable feature size, so the fabrication methodology requires changes from that of [23]. The system can instead be readily fabricated using standard photolithography. Microwave antennas and rectifiers are often fabricated utilizing machining with relatively large dimensions such that difficulties associated with microfabrication can be avoided. However, with careful design, issues introduced by microfabrication can be minimized.

Background

Metamaterial microwave rectennas such as the one presented in Almoneef et al. contain multiple layers of dielectric and metal planes with electrical connections between them. A vertical cross-section of this device design is shown in Figure F5.

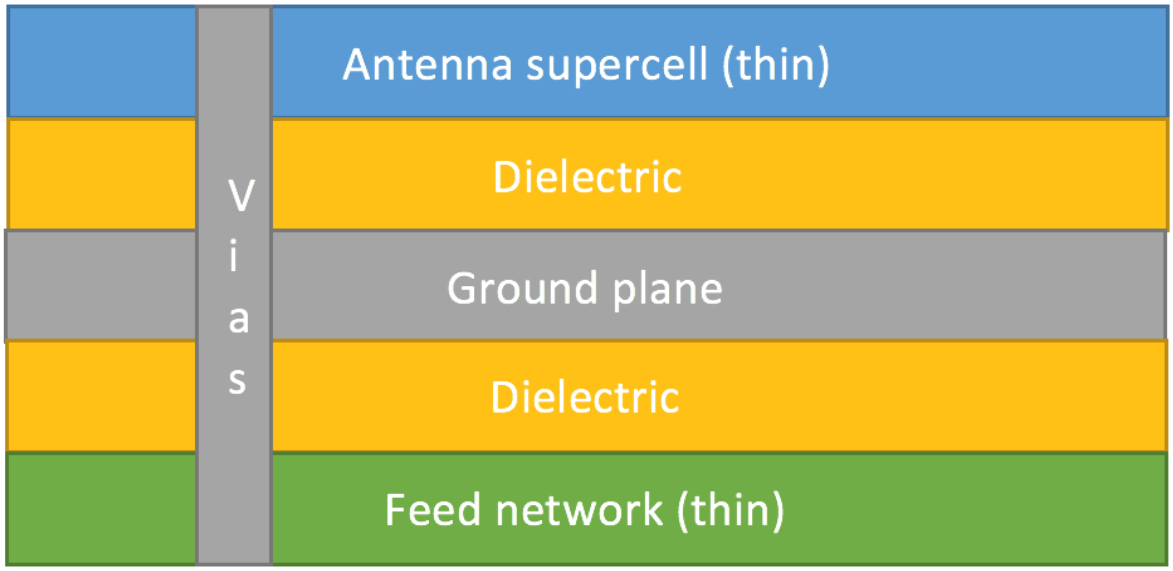

Figure F-5:Layers of device fabricated in [23]

The metamaterial antenna layer is a patterned metal, fabricated by machining. It is a thin layer (35 µm) that can be considered a 2D coating on top of a much thicker dielectric layer. This is the surface that captures the microwave radiation. The dielectric layer below the antenna tunes the impedance of the structure to match that of free-space. Almoneef et al. [23] found an optimum thickness of 3.175 mm. Below this first dielectric is a metal ground plane that is used to isolate the antenna from the feed network and to prevent the incident radiation from interfering with the feed network and rectification circuitry. Beneath the ground plane is another dielectric with a thickness of 1.524 mm, below which a thin metal feed network is machined. The feed network is composed of microstrip transmission lines which consist of the ground plane, dielectric, and patterned metal together. The feed network also attaches to part of the matching network used to match impedance of the antenna and feed network to the rectification circuit. Therefore, this design has the feed network and antenna sharing the common central ground plane. Finally, this design contains a via that connects the antenna to the feed network through the dielectric and ground plane layers and is electrically isolated from the ground plane.

Design for Photolithographic Fabrication

Since photolithography is required to fabricate this project's design, changes were made to ensure compatibility with the technology. There are three major challenges associated with the translation of traditional metamaterial microwave rectenna designs to a photolithographic process.

The first challenge is the creation of conductive vias between the antenna and feed network, since these vias pass through a metal ground plane but must be electrically isolated from the ground plane. Creating electrically isolated current pathways through two dielectric layers and a ground introduces significant complexity into a photolithographic protocol.

The second challenge is the fabrication of the feed network. Since photolithography requires deposition and patterning of layers that are placed on top of a substrate, it is extremely difficult to fabricate a network on the backside of the device. Due to this constraint, the traditional metamaterial rectenna layout comprising of the feed network, antenna, and their respective dielectric layers sandwiching a central ground plane would be a formidable challenge to fabricate via photolithography. The feed network must also be connected to a matching network which must be accessible to probes, generally contacting the top of the device. Contacts on the feed network or matching network would be inaccessible if they were on the bottom layer of the device.

The third challenge is the attachment of discrete circuit components to the matching network. Due to the scale down of geometry, soldering these components to make electrical connections becomes more difficult. Additionally, attaching these components would not be possible if the matching network is between the dielectric and substrate layers.

Due to these significant challenges with the fabrication of the vias and feeding network, it was determined that a modified design to circumvent these features was required. The goal of this design was to produce a rectenna system which includes the antenna and feed network on the same plane to eliminate the need for vias and the complications associated with fabrication of the sandwiched ground plane design of traditional metamaterial antennas.

The new design incorporates the metamaterial antenna supercell and the feed network on one plane. The design has each two feed networks connected to different components to separately feed the two distinct polarizations of light that are absorbed by the different components. Figure F6a) shows a not-to-scale schematic of the design. As in [23], the first and third columns of components are connected to the feed network by the side to collect for the first polarization while the second and fourth columns of components are connected to the feed network by the top to collect the second polarization. The two large squares at the end of the feed networks are 0.5 mm by 0.5 mm contacts for testing microwave absorption by the supercell, which will be evaluated in the first fabrication run. The to-scale drawings of the antenna components are shown in Figure F6b), the supercell in Figure F6c), the feed network in Figure F6d), and the supercell and feed network together in Figure F6e). Measurements shown are in millimeters.

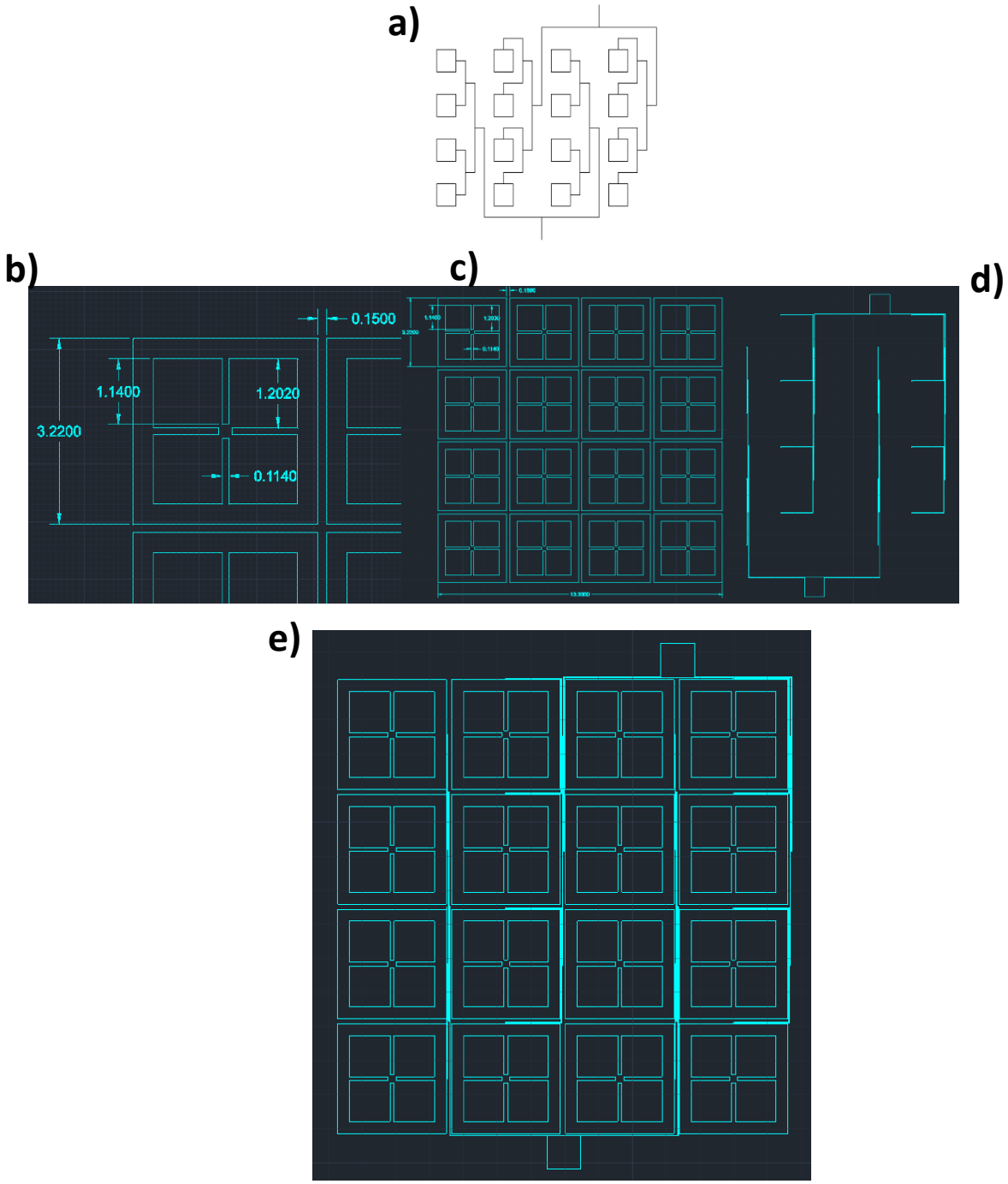

Figure F-6: a) the design of the feeding network (not to scale). b) a single antenna component (measurements in millimeters). c) the entire supercell (measurements in millimeters). d) the feed network to scale. e) the supercell and feed network on the same plane.

Fabrication Protocol

Deposition of copper will be done by e-beam evaporation on the IntIvac Nanochrome Deposition System available in the CIFRE cleanroom. Deposition of silica will be done by PECVD on the Trio Orion Plasma Enhanced Chemical Vapor Deposition System also available in the CIFRE cleanroom. Photolithography will be performed either in the CIRFE cleanroom, or in the undergraduate cleanroom supervised by Rossitza

Ivanova. CIFRE also has a flip-chip bonder, which we will use to solder discrete flip-chip circuit elements (diodes and capacitors) onto our devices. This will mediate the challenge of attaching circuit elements to the matching network. The facility also has RF characterization capabilities which we might take advantage of in addition to the capabilities of our supervisor's laboratory.

Safety

One of the top-priority requirements for this device is that it does not pose any safety risks for the wearer. With the radiation power constraints addressed, the remaining safety consideration is the material interfacing between the device and the user. In order to avoid conducting materials being in contact with biological tissues, which would pose serious hazards of electrical shock and oxidation of materials, the device must be coated in a biocompatible, corrosion resistant material. This safety consideration would be addressed by the manufacturer of the implantable biosensor that would contain the powering unit. The implant designs consist of a biocompatible enclosure, which would encapsulate the powering unit. Thus, this requirement does not set constraints on materials or design for the powering unit.

Cost

A functional requirement specifies low cost for the final product. In order to meet this requirement, we have chosen cheap materials including copper and silicon. Low cost bulk production of antennas will be achieved through the use of scalable microfabrication techniques including standard photolithography (with a reusable mask) and metal sputtering.

Appendix G: Verification Data

Reproduction of previous work

COMSOL

In [23], the radiation to AC conversion efficiency simulation was conducted in HFSS. In order to validate simulation methods, these results were reproduced in COMSOL. After performing this exercise, confidence in the validity of the modified design's simulation in the following section increased significantly. Quantities of interest in this simulation include the absorption of incident radiation, and the efficiency of power transfer to resistive loads (as a function of frequency of the incident waves). The resistive loads are a lumped element representation the impedance of the matching and feeding network that will be connected to the absorber, and to which the absorbed power is to be channelled.

In the simulation, the sides of the super cell were given periodic boundary conditions, mimicking an infinite metasurface. The surface is excited by a uniform port boundary condition set above it, to act as a source of microwave radiation of a single polarization having a power level of 1W. Adjacent antennas are electrically isolated from one another by regions containing no deposited metal. The boundary condition above the metasurface is a perfectly matched layer (PML) intended to absorb any reflected wave such that an accurate approximation of the radiation absorbed by the antenna can be obtained. The boundary condition below the substrate is a perfect electric conductor (PEC) which models a ground plane, which reflects any incident radiation. The frequency of the radiation generated by the port is swept to observe the behaviour of the absorber around its operating frequency. The simulations are performed for two orthogonal polarizations to verify the dual-polarization capabilities of the design. The simulation setup is shown in Figure G1.

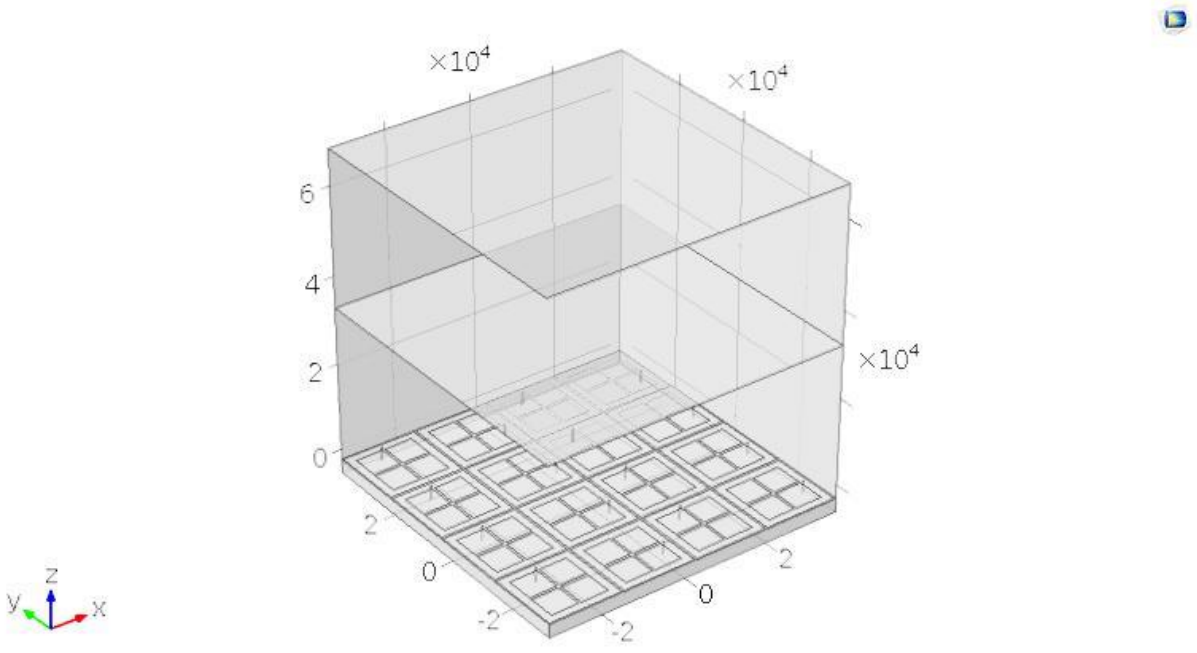

Figure G-1: Simulated structure (units of µm). Supercell is shown on top of a layer of dielectric backed by a PEC. On top of the metamaterial is an air box, at the top of which is the source excitation, and a PML air box.

The absorption was calculated using scattering parameters (S-parameters) with the following expression, where $|S_{33}|^2$ is the reflection coefficient of the source port (Port 3). A low reflection coefficient is indicative of high absorption, which is reflected in the expression above. Figure G2 compares the original and reproduced absorption of the design around the operating frequency. The reproduced absorption is very similar to that presented in [23] for both polarizations in that they have similar resonant frequencies and absorption efficiencies at those frequencies.

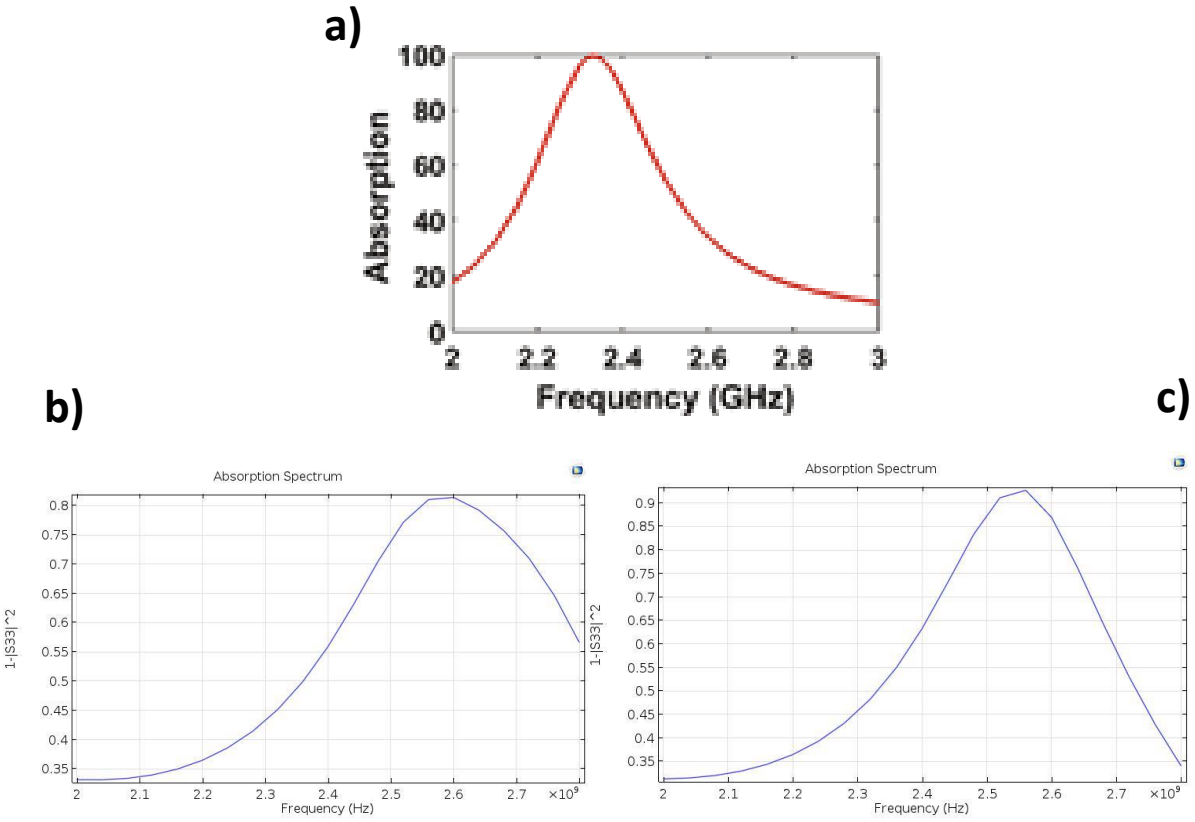

Figure G-2: a) Absorption spectrum from [23]; the plots for both polarizations are very similar, so only one polarization is shown. b) Reproduced absorption spectrum for polarization 1. c) Reproduced absorption spectrum for polarization 2.

In energy harvesting applications, it is important to also measure the power transfer efficiency, since the channelling of absorbed power is just as critical as the absorption. In [23], the efficiency is defined as the ratio of the total energy dissipated across all 16 resistors of each cell to the incident power. In the COMSOL simulations, this was reproduced as the transmission coefficient between the Port 3 (the source) and Ports 1 and 2, which are the feeding points for each of the two polarizations – $|S_{13}|^2$ and $|S_{13}|^2$, respectively. The reproduced figures (Figure G3) are very similar to those in [23]. Furthermore, the reproduced plots exhibit the expected dual-polarization behaviour, as for a given polarization of the incident radiation, only one port exhibits significant absorption. The figure also verifies the strong coupling between the unit cells, as the efficiencies are relatively high.

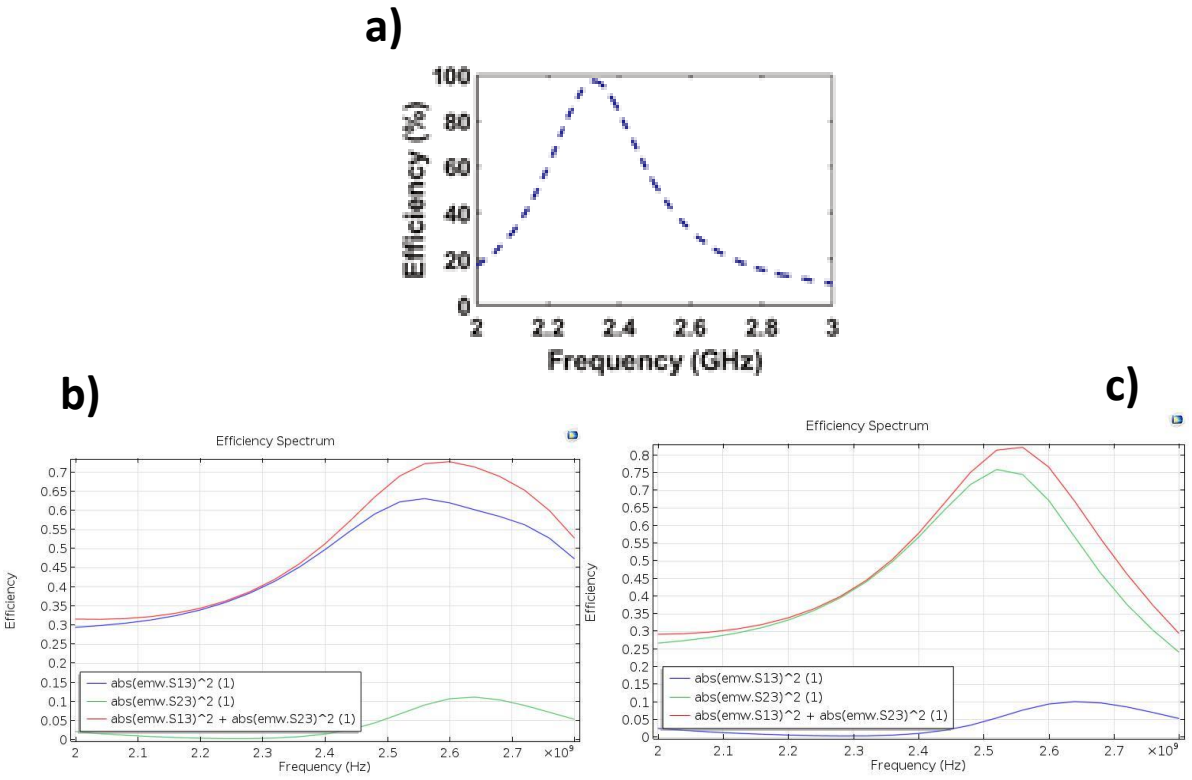

Figure G-3: a) Efficiency spectrum from [23]; the plots for both polarizations are very similar, so only one polarization is shown. b) Reproduced efficiency spectrum for polarization 1. c) Reproduced efficiency spectrum for polarization 2.

Additionally, the surface plot of the electric field intensity on the metamaterial generated in COMSOL is compared to that published in [23]. The reproduced plots are shown in Figure G4. Upon examination of Figure G4, it is evident that the reproduced simulation exhibits the expected dual-polarization operation. Figure G4a) is irradiated with waves in polarization 1 and shows that only the associated unit cells absorb the incident light. Similarly Figure G4b) is irradiated with a wave in polarization 2 and displays the unit cells with orthogonally placed vias absorbing the energy.

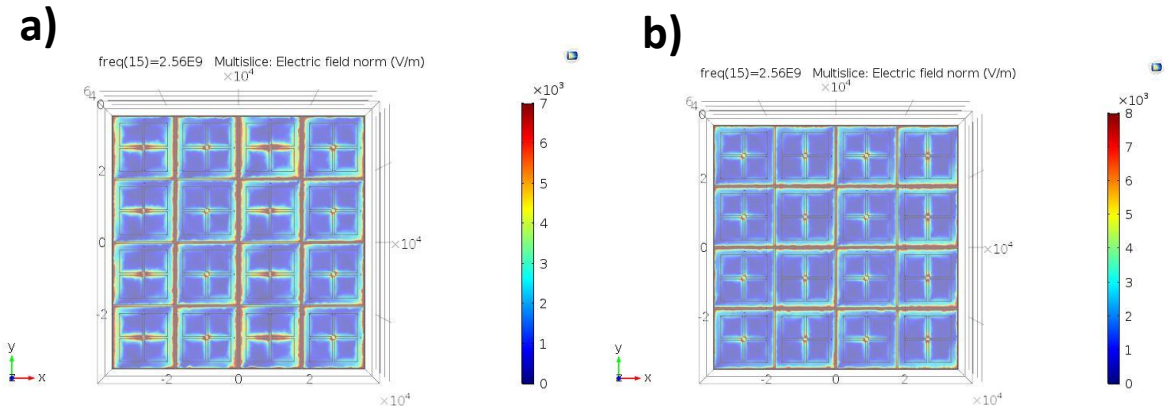

Figure G-4: a) Reproduced surface plot of the magnitude of the electric field at the resonant frequency for polarization 1. b) Reproduced surface plot of the magnitude of the electric field at the resonant frequency for polarization 2.

ADS

In order to model the AC to DC conversion process, Advanced Design System (ADS) software was used. The matching networks for each polarization from [23] were implemented in the software, which included transmission line dimensions and circuit components. A 1-tone frequency power source was used to represent the output from super-cell system obtained from the COMSOL simulation of the metamaterial. Impedance values obtained from the COMSOL full-wave simulation were extracted and imported into ADS, creating a frequency-dependent impedance of the power source representing the metamaterial antenna. A series HSMS 2860 Schottky diode was used for the rectification for its low turn-on voltage at the frequency of operation. A capacitor was implemented in series with a load resistor for low-pass filtering of the signal. Transmission lines were simulated as microstrip lines with dimensions specified in [23]. A large signal S-parameter (LSSP) simulator was used to analyse the reflection coefficient of the rectifier for each polarization. The S_{11} parameter is related to the reflection coefficient of the source port radiating a wave with polarization 1, and the S_{22} parameter is related to the reflection coefficient of the source port radiating a wave with polarization 2. The schematic in Figure G5 depicts this matching network, where TL are transmission lines, with lengths defined in [23].

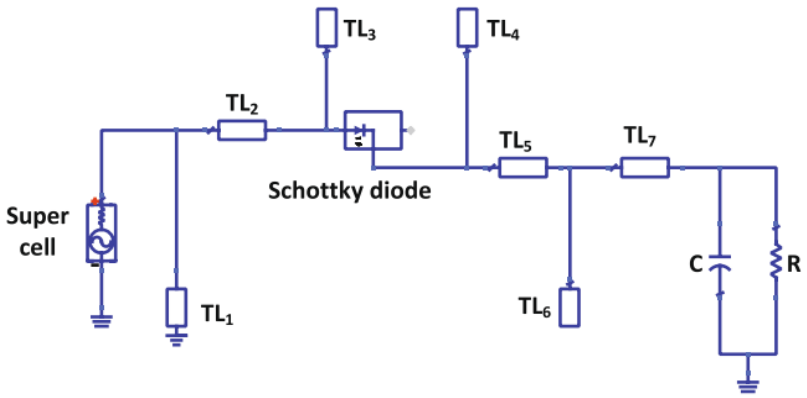

Figure G-5: Schematic of matching network in ADS [23]

Two figures demonstrating the device were reproduced from [23] to demonstrate the validity of our simulations. Figures G6a-b) show S-parameters (related to the reflection coefficients) as a function of source frequency, and the Figures G6c-d) show the AC to DC conversion efficiency (determined by the percentage of input power dissipated across a resistive load), vs. source frequency. This demonstrates that the current ADS simulation can reliably reproduce the previous work.

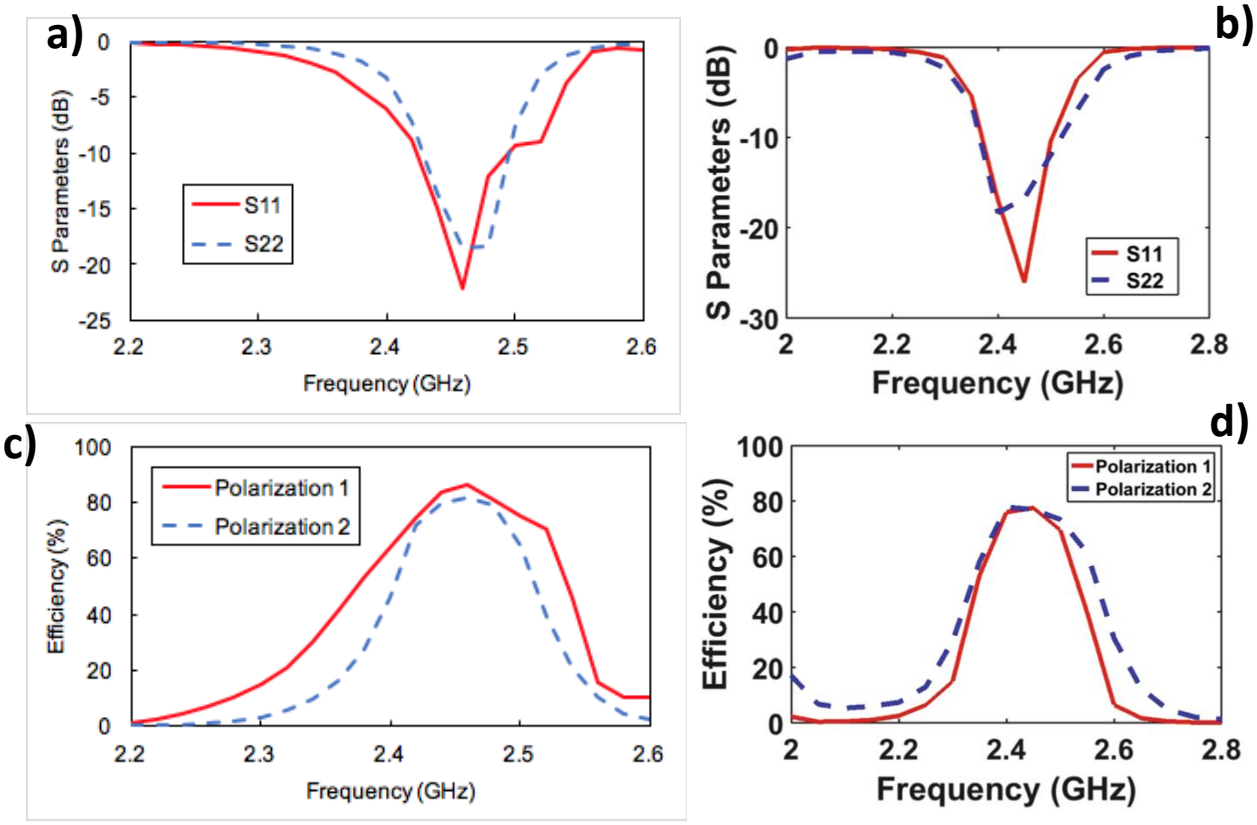

Figure G-6: a) S-parameter vs. frequency plot for each polarization from [23]. b) Reproduced S-parameter vs. frequency plot for each polarization. c) Efficiency vs. frequency plot for each polarization from [23]. d) Reproduced efficiency vs. Frequency plot for each

Scaled-down design – COMSOL

A few modifications to the design presented in [23] were made to meet the design specifications. FR4 is not a commonly available material for deposition, therefore silica (SiO_2) was selected as the dielectric spacer instead. The dielectric constant of FR4 (2.2) is roughly half that of silica (4.2). Therefore, the refractive index of the dielectric material is increased by a factor of approximately 2. Thus, in order for the system to have the same dynamics, the dielectric thickness should be reduced by a factor of 2 (such that the index normalized optical path length traversed by a wave of given energy remains constant). Additionally, in order to decrease the size of the system, an operating frequency of 12 GHz was chosen. Therefore, all geometrical dimensions were scaled by a factor of roughly 0.2 (after adjusting for the material change). Exact dimensions were adjusted by trial and error such that the peak absorption frequency occurs at 12 GHz.

Upon scale-down of the system, the absorption peak was diminished to a value of about 0.6. This is because the impedance of the antenna shifted as the dimensions were scaled down, and therefore the antenna elements were not impedance matched with the lumped port feeding them. Thus, the impedance of the lumped port was swept and an optimal value of 60 Ω was found (Figure G7).

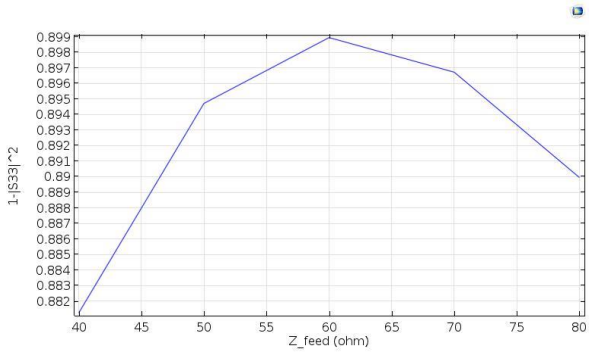

Figure G-7: Lumped port impedance sweep for scaled down system

Given the dimensions of the system at this point in the simulation, it was determined that more space was needed in between antenna elements in order to properly feed them. Therefore, a simulation was run with increased spacing between elements, and the results showed an increase in the peak absorption frequency. Upon rescaling of the system around a peak absorption frequency of 12 GHz, a set of reasonable geometrical parameters (detailed in Table G1) was obtained with good absorption and efficiency properties (Figure G8 and G9. The electric field distribution at the resonant frequency is pictured in Figure G10.

Table G-1: Dimensions for scaled-down design (see Figure F1 for parameter definitions)

Parameter	Value
d	3.22 mm
w_1	0.114 mm
w_2	0.351 mm
S	150 µm
P	13.5 mm
l_c	1.14 mm

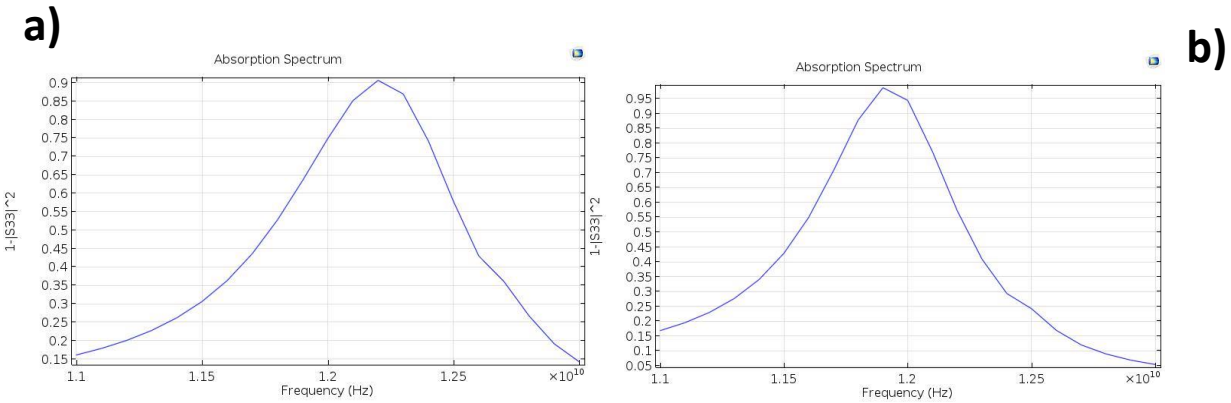

Figure G-8: a) Polarization 1 absorption spectrum. b) Polarization 2 absorption spectrum.

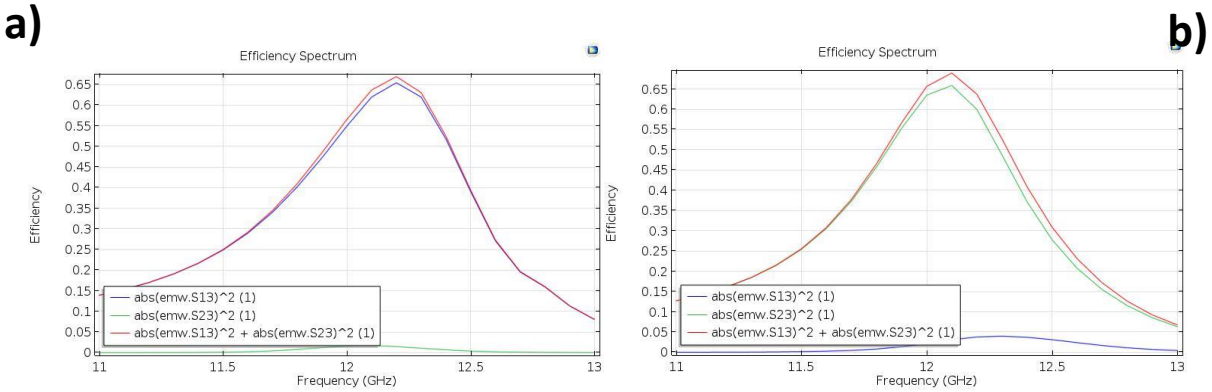

Figure G-9: a) Polarization 1 efficiency spectrum. b) Polarization 2 efficiency spectrum.

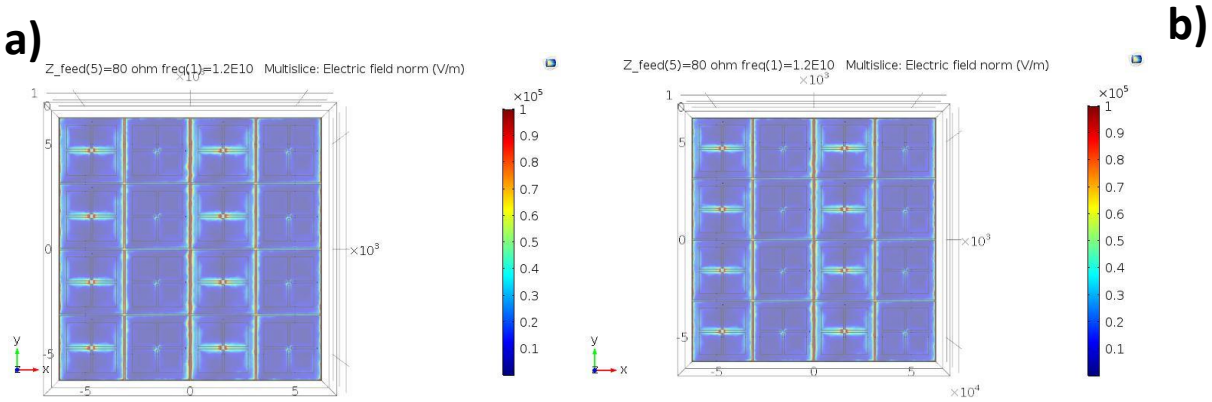

Figure G-10: a) Polarization 1 electric field. b) Polarization 2 electric field.

Another figure of merit used to verify the impedance matching of the antenna to free space is the voltage standing wave ratio (VSWR). The VSWR is a measure of impedance matching of a component and a waveguide, which in this case are the metamaterial absorber and free space respectively. Perfect impedance matching would result in perfect absorption of incident waves, while impedance mismatches would result in reflection of some incident power. Of course, the fraction of reflected radiation increases with increasing impedance mismatch. Reflected waves interfere with incoming incident radiation, forming standing waves. The VSWR is the ratio of maximum voltage to minimum voltage in the standing wave and varies from 1 to infinity, with 1 indicating perfect matching, and the value increasing with increased mismatching [27]. Figure G11 below shows the simulated VSWR as a function of frequency for both polarizations. The VSWR is very close to 1 around the operating frequency, confirming that the absorber is well matched.

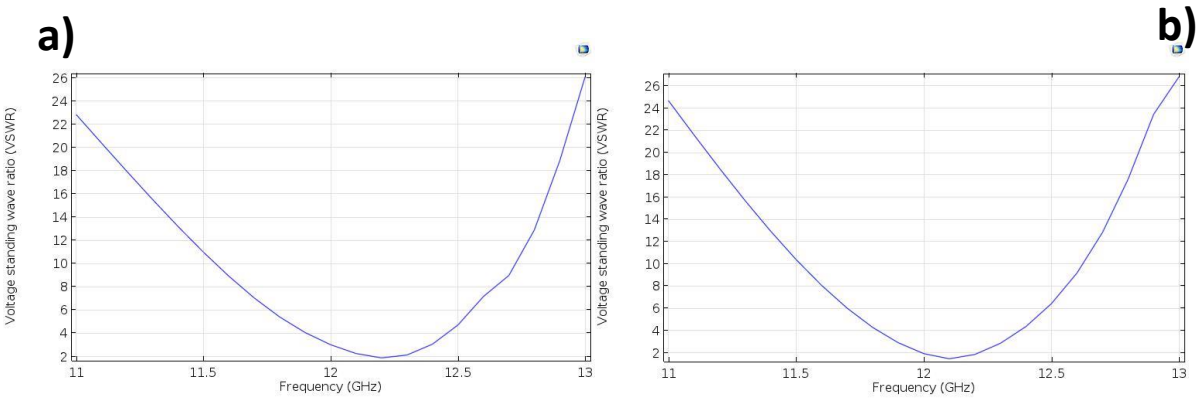

Figure G-11 : a) Polarization 1 VSWR. b) Polarization 2 VSWR

.

Appendix H: Prototype Test Data

First, the electrical connections between components and metal integrity of the antenna were verified using a DMM. The fact that a current was measurable between the probes indicated that the antenna metal was connected throughout and the leads of the components (diodes and capacitors) were connected to the antenna metal. Then DMM measurements were performed to validate the built-in voltage of the diode and the capacitance of the chip capacitor was measured with an LCR meter. A built-in voltage of 0.72 V was measured across the diode and a capacitance of 2.86 nF was measurable across the capacitor, both of which match up well with the diode and capacitor specifications [28, 29].

The receiving characteristics of the device were measured in an anechoic chamber to minimize the presence of background microwave radiation. The terminals of the coplanar striplines were connected to a DMM via alligator clips, the intention was to measure a DC voltage across the terminals when microwaves of the appropriate frequency were incident on the structure. A horn antenna was connected to a signal generator and a microwave signal was sent from the horn antenna through free space to the rectenna system. A sweep of frequencies between 3 and 10 GHz was performed as well as power levels between -10 dBm and 25 dBm. Several different separation distances between 30 cm and 80 cm were also tested, as well as two different polarizations of the incoming radiation. Throughout testing the voltage reading on the DMM was zero.

Figure H-1: a) Backing for device testing. b) Close-up of device probing for measurement. c) Horn antenna. d) Anechoic chamber setup

References

[1] U.S. Food and Drug Administration, "Paving the Way for Personalized Medicine," October 2013.

[2] S. Sirivisoot, "Biosensors as Implantable Medical Devices for Personalized Medicine," *Journal of Biosensors & Bioelectronics,* vol. 3, no. 2, p. 1, March 2012.

[3] C. Walker, "Surpassing the Limits of Battery Technology," 4 November 2016. [Online]. Available: https://chemical-materials.elsevier.com/chemical-manufacturing-excellence/surpassing-limits-battery-technology/?fsdsd=efwe.

[4] C. Liu, Y. X. Guo, H. Sun and S. Xiao, "Design and Safety Considerations of an Implantable Rectenna for Far-Field Wireless Power Transfer," *IEEE Transactions on Antennas and Propagation,* vol. 62, no. 11, pp. 5798-5806, November 2014.

[5] E. Donchev, "The rectenna device: From theory to practice (a review)," *MRS Energy & Sustainability,* vol. 1, January 2014.

[6] Consumer and Clinical Radiation Protection Bureau, "Limits of Human Exposure to Radiofrequency Electromagnetic Energy in the Frequency Range from 3 kHz to 300 GHz," 2015. [Online]. Available: https://www.canada.ca/en/health-canada/services/environmental-workplace-health/consultations/limits-human-exposure-radiofrequency-electromagnetic-energy-frequency-range-3-300.html#s2.

[7] H. Rahmani and A. Babakhani, "A Fully Integrated Electromagnetic Energy Harvesting Circuit with an On-Chip Antenna for Biomedical Implants in 180 nm SOI CMOS," in *SENSORS, 2016 IEEE*, Orlando, FL, 2016.

[8] W.-H. Tu, S.-H. Hsu and K. Chang, "Compact 5.8-GHz Rectenna Using Stepped-Impedance Dipole Antenna," *IEEE Antennas and Wireless Propagation Letters,* vol. 6, pp. 282-284, 2007.

[9] A. Ben Amar, A. B. Kouki and H. Cao, "Power Approaches for Implantable Medical Devices," *Sensors,* vol. 11, pp. 28889-28914, November 2015.

[10] Medical Device and Diagnostic Industry, "Medical Device Batteries: Smaller is Better," 22 August 2014. [Online]. Available: https://www.mddionline.com/medical-device-batteries-smaller-better. [Accessed March 2018].

[11] M. Hotta, M. Hayashi, A. Nishikata and K. Nagata, "Complex Permittivity and Permeability of SiO2 and Fe3O4 Powders in Microwave Frequency Range between 0.2 and 13.5 GHz," *ISIJ Internationsl,* vol. 9, no. 49, pp. 1443-1448, January 2009.

[12] R. Ivanova, *Nanotechnology Engineering Advanced Laboratory 2: MEMS devices: fabrication and testing - Winter 2018 Lab Manual,* Waterloo, Ontario: University of Waterloo, 2018.

[13] F. Gong, P. Swain and T. Mills, "Wireless endoscopy," *Gastrointestinal Endoscopy,* vol. 51, no. 6, pp. 725-729, June 2000.

[14] P. Jourand and R. Puers, "An Autonomous, Capacitive Sensor Based and Battery Powered Internal Bladder Pressure Monitoring System," *Procedia Chemistry,* vol. 1, no. 1, pp. 1263-1266, September 2009.

[15] "Under the skin, a tiny laboratory," Ecole polytechnique fédérale de Lausanne, 20 March 2013. [Online]. Available: https://actu.epfl.ch/news/under-the-skin-a-tiny-laboratory/.

[16] A. Darwish and A. Hassanien, "Wearable and Implantable Wireless Sensor Network Solutions for Healthcare Monitoring," *Sensors,* vol. 11, pp. 5561-5595, 26 May 2011.

[17] U.S. Food and Drug Administration, "Overview of Device Regulation," [Online]. Available: https://www.fda.gov/MedicalDevices/DeviceRegulationandGuidance/Overview/default.htm.

[18] International Trade Administration, "Medical Device Regulatory Requirements for Canada," June 2011. [Online]. Available: https://www.trade.gov/td/health/canadamdprofile.pdf.

[19] Boston Scientific, "Accolade Pacemakers Brochure," [Online]. Available: https://www.trade.gov/td/health/canadamdprofile.pdf.

[20] A. H. M. Furqan, "Surface Area in Children: A Simple Formula," *Indian Pediatrics,* vol. 46, 17 December 2009.

[21] "The Average Weight of a Newborn," LiveStrong, 6 February 2014. [Online]. Available: https://www.livestrong.com/article/197126-normal-weight-of-a-newborn/.

[22] R. P. P. Jourand, "An Autonomous, Capacitive Sensor Based and Battery Powered Internal Bladder Pressure Monitoring System," *Procedia Chemistry,* vol. 1, no. 1, pp. 1263-1266, September 2009.

[23] T. S. Almoneef, F. Erkmen and O. M. Ramahi, "Harvesting the Energy of Multi-Polarized Electromagnetic Waves," *Scientific Reports,* vol. 7, 16 October 2017.

[24] W. Tang and T. Au-Yeung, "Measure a Voltage Standing Wave Ratio (VSWR) to Quantify Transmission Line Imperfections," Maxim Integrated, 2016. [Online]. Available: https://www.maximintegrated.com/en/app-notes/index.mvp/id/5432. [Accessed March 2018].

[25] H. Sun, Y. X. Guo, M. He and Z. Zhong, "Design of a High-Efficiency 2.45-GHz Rectenna for Low-Input-Power Energy Harvesting," *IEEE Antennas and Wireless Propagation Letters,* vol. 11, pp. 929-932, 2012.

[26] H. Mashaal and J. M. Gordon, "Efficiency limits for the rectification of solar radiation," *Journal of Applied Physics,* May 2013.

[27] Microwaves101, "Voltage standing wave ratio (VSWR)," [Online]. Available: https://www.microwaves101.com/encyclopedias/452-vswr.

[28] Macom, *MA4Exxxx Series - GaAs Schottky Barrier Diodes.*

[29] *Chip Monolothic Ceramic Capacitor for General - Reference SHeet.*